THESIS WORK FOR DUAL MASTER'S DEGREE

KIT M.Sc. in Mechanical Engineering

ITBA Mag. in Energy and Environment

CONCEPT AND DESIGN OF A HIGH POWER DENSE PROPULSION SYSTEM FOR ELECTRIC AIRCRAFT

Lennart Beneke
Mechanical Engineering - KIT

Tutor
M.Sc. Steffen Reuter, FRAUNHOFER ICT

Co-Tutor
Dr.-Ing. Lars-Fredrik Berg, FRAUNHOFER ICT

Examiners
Prof. Dr.-Ing. Frank Henning, KIT/ FAST
Prof. Dr.-Ing. Luise Kärger , KIT/ FAST
Prof. Dr.-Ing. Robert Stieglitz KIT/ ITES

Karlsruhe
02/10/2023

Institute of Vehicle System Technology
Lightweight Design
Prof. Dr.-Ing. Luise Kärger
Prof. Dr.-Ing. Frank Henning

Rintheimer Querallee 2
76131 Karlsruhe

Master Thesis

Concept and Design of a High Power Dense Propulsion System for Electric Aircraft

Lennart Beneke

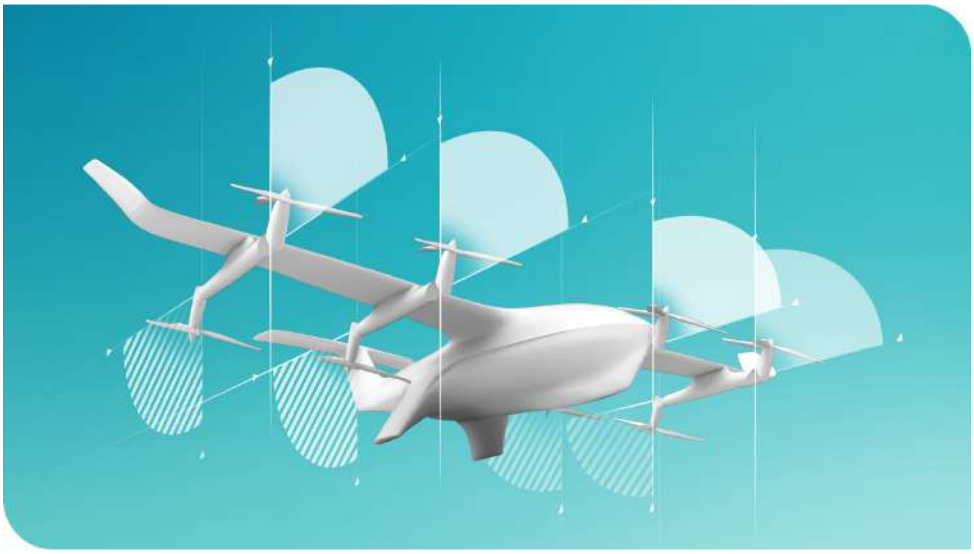

Supervisor: Steffen Reuter M. Sc.
Fraunhofer ICT

No.: 23-L-0015

Karlsruhe, October 2023

Institute of Vehicle System Technology
Lightweight Design
Prof. Dr.-Ing. Luise Kärger
Prof. Dr.-Ing. Frank Henning

Rintheimer Querallee 2
76131 Karlsruhe

Auslegung und Konstruktion eines leistungsdichten Antriebsgondelsystems für elektrische Luftfahrzeuge

Concept and Design of a High Power Dense Propulsion System for Electric Aircraft

Lennart Beneke
Matr.-Nr.: 1962987

The master's thesis is to be prepared in close contact with the institute. All copies given to the institute become the property of the institute. Third-party inspection may only take place after consultation with the institute.

Issue Date:	01.04.2023	Due Date:	02.10.2023

Supervisor:

(Prof. Dr.-Ing. Frank Henning)

(Prof. Dr.-Ing. Luise Kärger)

Project Leader:

(Dr.-Ing. Lars-Fredrik Berg - Fraunhofer ICT)

(M. Sc. Steffen Reuter - Fraunhofer ICT)

Author:

(Lennart Beneke)

Adress:

City	Karlsruhe
Street	Schützenstraße 16
Phone	+49176 45956763

Institute of Vehicle System Technology
Lightweight Design
Prof. Dr.-Ing. Luise Kärger
Prof. Dr.-Ing. Frank Henning

Rintheimer Querallee 2
76131 Karlsruhe

Task Description
for
Mr. Lennart Beneke
(Matr.-No.: 1962987)

Auslegung und Konstruktion eines leistungsdichten Antriebsgondelsystems für elektrische Luftfahrzeuge

Concept and Design of a High Power Dense Propulsion System for Electric Aircraft

Within the scope of the ALBACOPTER® Lighthouse Project, novel drive systems for eVTOL are being designed, demonstrated and tested. While direct drive systems are commonly used in the field of electric take-off and landing(eVTOL) aircrafts today, the Fraunhofer engineers have deliberately chosen an alternative path towards realizing a drive system with higher performance. The aim is to develop a geared drive system with a higher weight-specific power output for the ALBACOPTER® 1.0. All relevant constraints have to be identified and investigated based on the state of the art and relevant regulations in order to develop a concept for a tiltable geared drive unit. Particularly, the effects of aerodynamic loads caused by oblique propeller inflow should be considered as they are impactful factors. A methodology for estimating these loads should be identified and used. Consequently, a drive and tilt topology can be established based on the obtained results.

Declaration

I hereby declare that I have prepared this thesis independently and only with the sources and aids indicated in the bibliography.

Karlsruhe, October 2, 2023

Abstract

The present thesis proposes a conceptual design of a tiltable propulsion system for the ALBACOPTER® 1.0, an eVTOL aircraft with a take-off mass of800 kg. Usually, the propulsion systems of eVTOLs are direct drives due to their simple design. However, since the propeller thrust in relation to the take-off mass is the most important criterion for vertical take-off aircraft, power-dense drives are of maximum importance. Therefore, a propeller drive concept combining a high-performance synchronous machine with a gearbox is developed and investigated with regard to its performance. For this purpose, all boundary conditions are determined. First, the propeller is simulated in order to define its relevant speeds and gear's reduction ratio. Then the aerodynamic loads are estimated using data from wind tunnel tests and CFD simulations and qualitatively compared with own wind tunnel tests. It is shown that the moments induced by oblique propeller inflow play a significant role compared to the lateral forces. By calculating and classifying these and other potential loads, concepts for the drive train and the tilt actuator are developed and evaluated.

Kurzfassung

Die vorliegende Arbeit befasst sich mit der Auslegung und Konzeptionierung eines schwenkbaren Antriebssystems für den ALBACOPTER® 1.0, einem eVTOL-Fluggerät mit 800 kg Abflugmasse.

Üblicherweise sind die Antriebssysteme von eVTOLs aufgrund ihrer einfachen Bauweise Direktantriebe. Da für senkrechtstartende Flugzeuge der Propellerschub in Relation zur Abflugmasse jedoch das wichtigste Kriterium darstellt, sind leistungsdichte Antriebe von maximaler Wichtigkeit. Daher soll ein Propellerantriebskonzept, das eine Hochleistungssynchronmaschine mit einem Getriebe kombiniert, entwickelt und hinsichtlich seiner Leistungsfähigkeit untersucht werden. Dafür müssen sämtliche Randbedingungen bestimmt werden. Zuerst wird der Propeller simulativ untersucht, um die relevanten Drehzahlen und die Getriebeübersetzung definieren zu können. Dann werden die aerodynamischen Lasten anhand von Daten aus Windkanalversuchen und CFD-Simulationen abgeschätzt und mit eigenen Windkanalversuchen qualitativ verglichen. Dabei zeigt sich, dass die durch schräge Propelleranströmung induzierten Momente im Vergleich zu den Seitenkräften eine bedeutende Rolle spielen. Mit der Berechnung und Einordnung dieser und weiterer potenzieller Lasten werden Konzepte für den Antriebsstrang und den Schwenk-Aktuator entwickelt und bewertet.

Contents

Abbreviations

Abbreviation	Meaning
BET	Blade Element Theory
BLDC	Brushless Direct Current
eVTOL	Electric Vertical-Takeoff-and-Landing
CFD	Computational Fluid Dynamics
FM	Figure of Merit
Hil	Hardware in the Loop
ICAO	International Civil Aviation Organization
ICT	FRAUNHOFER INSTITUTE FOR CHEMICAL TECHNOLOGIES
LoI	Letter of Intent
NACA	National Advisory Committee for Aeronautics
NASA	National Aeronautics and Space Administration
NAS	New Drive Systems Department (German: Neue Antriebssysteme)
OEI	One Engine Inoperative
PIV	Particle Image Velocimetry
PMSM	Permanent Magnet Synchronous Machine
UAM	Urban Air Mobility
UAV	Unmanned Aerial Vehicle

1 Introduction

This chapter depicts the ALBACOPTER® project, motivates the present thesis, gives an overview of the initial situation of the project and outlines its evolution during this thesis.

1.1 The FRAUNHOFER Lighthouse Project ALBACOPTER®

Within the ALBACOPTER® Lighthouse Project led by FRAUNHOFER IVI, an airborne experimental platform is developed and approved for testing and demonstration flights that combines the VTOL capabilities of multicopters with the aerodynamic advantages of gliders. The ambitious project incorporates six Fraunhofer Institutes' expertise and technologies from the fields of mobility, materials science, energy and propulsion engineering, mechatronics, as well as sensor, communication and automation technology, artificial intelligence and production engineering. [1]

The project comprehends three scales of vectored-thrust eVTOL aircrafts. The ALBACOPTER® 0.1 was a commercial drone with about 3m wingspan. The ALBACOPTER® 0.5 will have 7 m wingspan and is currently under construction. At the same time the third stage, the ALBACOPTER® 1.0, is being designed. It's designed for a Maximum Take-Off Weight (MTOW) of 800 kg and a wingspan of 14 m. A first design study of the ALBACOPTER® 1.0 is shown in figure 1.1.

The NEW DRIVE SYSTEMS DEPARTMENT (NAS) at FRAUNHOFER ICT (FRAUNHOFER INSTITUTE FOR CHEMICAL TECHNOLOGY) is responsible for the drivetrain of the self-devoloped UAVs.

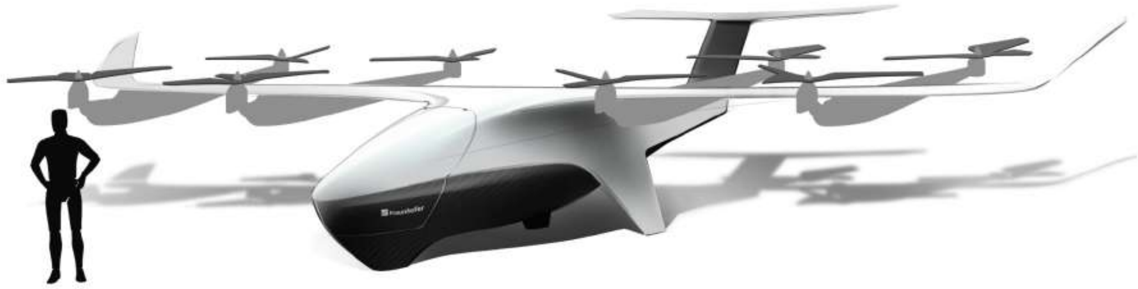

Fig. 1.1: First ALBACOPTER® 1.0 design study

1.2 Motivation

Many companies are currently developing eVTOL aircraft of considerable size for various purposes, such as urban transportation, medical transport, and Search-And-Rescue missions.

Commercial small drone technology commonly uses brushless air cooled outrunner motors. For larger electric motors, liquid cooling is a more viable option since the area that is relevant to air cooling does not increase in the same order of magnitude as the power. Therefore, scaling up small drone tech is not a feasible option.

An additional increase in power density can be achieved by the use of a gearbox. As electric motors of high rotational speed have imminently a higher power density than low-speed motors, there is a weight difference that increases approximately linear with power. However, the weight of a gearbox does not increase in a linear course with power, so there must be a certain power limit, from which on a highspeed motor with gearbox can be lighter than a direct drive.

To test the propulsion system, the ALBACOPTER® team's vision is first to build a so called „iron bird“ as a testing platform, similar to the one NASA used for the SCEPTOR project [2], both shown in figure 1.2.

a) b)

Fig. 1.2: a) NASA testbed [3] and b) FRAUNHOFER ALBACOPTER® 1.0 Iron Bird vision

1.3 Objective

While NASA is working on megawatt aerospace motors that achieve more than $13\,\mathrm{kW/kg}$ [4] [5], this work will focus on smaller motors. The goal is to design a propulsion system with at least $35\,\mathrm{kW}$ continuous and $50\,\mathrm{kW}$ peak performance. The power and torque density of available direct drive motors, shall be surpassed making use of a gearbox. In section 3.2.1 a market overview shows that available motors achieve about $3.5\,\mathrm{kW/kg}$ continuous performance density and about $13\,\mathrm{Nm/kg}$ continuous torque density.

There are some relevant criteria for the design of the propulsion system. First of all, it must be lightweight. For eVTOL applications the weight is even more important than for conventional aircraft, as every gram must be lifted by propellers during hover and transition, which are the most energy-consuming flight phases. Also, the design should be compact and have a small cross-section area to keep the aerodynamic drag low. Since the propulsion unit needs to be tiltable for hover and forward flight, a correct lubrication of the gears must also be ensured in every situation.

1.4 Starting Point - Pre-Defined Project Contents

The general concept (see figure 1.1) of the ALBACOPTER® 1.0 and a preliminary design and specifications are made by FRAUNHOFER IVI in Dresden. They defined the data given in table 1.1.

Tab. 1.1: Preliminary specifications of the ALBACOPTER® 1.0

MTOW	800	kg
Payload	200	kg
Wing Span	14	m
Cruise Speed	42.5	$\mathrm{m\,s^{-1}}$
Stall Speed	23	$\mathrm{m\,s^{-1}}$
Horizontal Climb Speed	32.5	$\mathrm{m\,s^{-1}}$
Vertical Climb Speed	4.5	$\mathrm{m\,s^{-1}}$
Number of Rotors	8	
Continuous Power (One Motor)	35	kW
Peak Power (One Motor)	50	kW

The required power calculation is based on a method described by Bruehl et al.[6] and includes some safety factors. Other aspects regarding the drivetrain were already specified internally, for example in the project proposal or as there are LoI (Letter of Intent) partners:

Motor Concept: A high speed permanent synchronous electric machine with customized design by SCIMO

Gear: A speed reducing gearbox

Propeller: 2-bladed HELIX H40 with TM profile and 1.75 m diameter

Propeller hub: The hub was designed in a previous master's thesis and contains a electrical pitch actuator (see Figure 1.3).

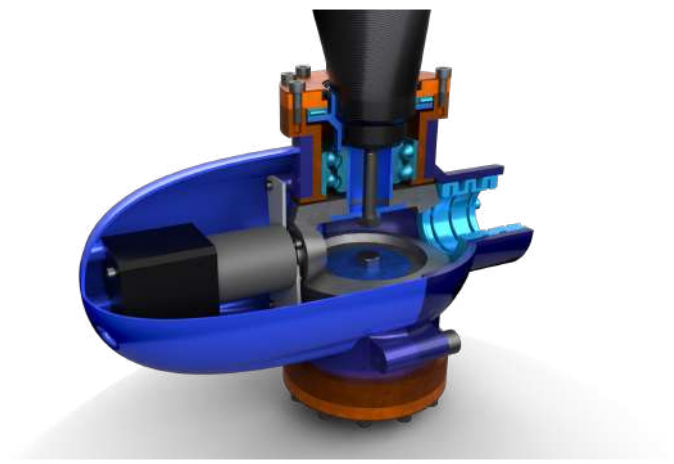

Fig. 1.3: Propeller Hub designed by Prinz [7]

Flight Mission Profile

A typical flight mission profile of an eVTOL, on which all assumptions are made, is depicted here.

Take Off: Vertical Take off and climb to transition altitude

First Transition: Acceleration, tilting propellers for transition to wingborne flight

Climb: Climb similar to conventional airplane

Cruise and Descent: Efficient flight in airplane mode at cruise speed

Second Transition: Deceleration, tilting propellers in vertical position until static hover is reached

Landing: Vertical descent and touchdown

1.5 Outline

This work begins with the fundamental knowledge about propellers, relevant phenomena for tilted rotors, and electric motors used in aviation. With this knowledge, technical solutions developed by eVTOL manufacturers are presented. Furthermore, relevant regulations for certification are provided. After completing these basic constraints, further limitations that are needed to design the propulsion system are investigated. Chapter 6 deals with aerodynamic and other possible loads that can occur to the propulsion system. Finally, the gained knowledge is applied to design different drivetrain and tilt actuation concepts, which are evaluated.

2 Fundamentals of Electric Aircraft Propulsion Systems

This chapter provides theoretical background about different aspects of propeller theory and some important phenomena for the following chapters. Afterwards, it outlines the fundamental knowledge about relevant electric motors used in aviation.

2.1 Propellers

In this section, the most relevant definitions and some knowledge about propellers are given. Furthermore, some phenomena and problems especially relevant for large-scale propellers and drivetrains that are crucial for eVTOL design are introduced. Finally the Blade Element Theory (BET), widely used for propeller performance calculations, is explained.

2.1.1 Coordinate System

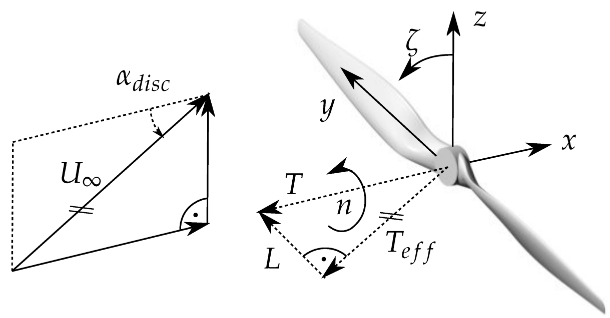

Fig. 2.1: Definition of the hub coordinate system [8]

The coordinate system used in this work is fixed on the propeller hub and independent of the inflow direction. The *x*-axis points in outflow direction. The inflow angle α_{disc} lies in the *xz* plane and is measured between the propeller shaft and and the air stream. The resulting thrust can be split under non-axial inflow into the effective thrust in inflow direction and lift perpendicular to the inflow.

When looking at a section of a propeller blade at radius r depicted in figure 2.2, the resulting inflow velocity U_{section} meets the airfoil at the angle off attack α_{section}. U_{section} is composed of the rotational velocity ωr, the freestream velocity U_{∞} and the axial and circumferential induced velocities, induced by the flow field. [8]

It is important to know that the local inflow velocity U_{Section} depends on the inflow angle α_{disc} and the propeller's azimuthal position ζ. Under lateral inflow, the advancing blade experiences a larger inflow velocity than the retreating blade and therefore produces more lift. This leads to the so-called „flapping moments".[9]

The resulting infinitesimal force $\mathrm{d}R$ can be split either along the the inflow vector into lift $\mathrm{d}L$ and drag $\mathrm{d}D$, or along the the rotational axis into the the thrust $\mathrm{d}T$ and torque component $\mathrm{d}Q/r$. [8]

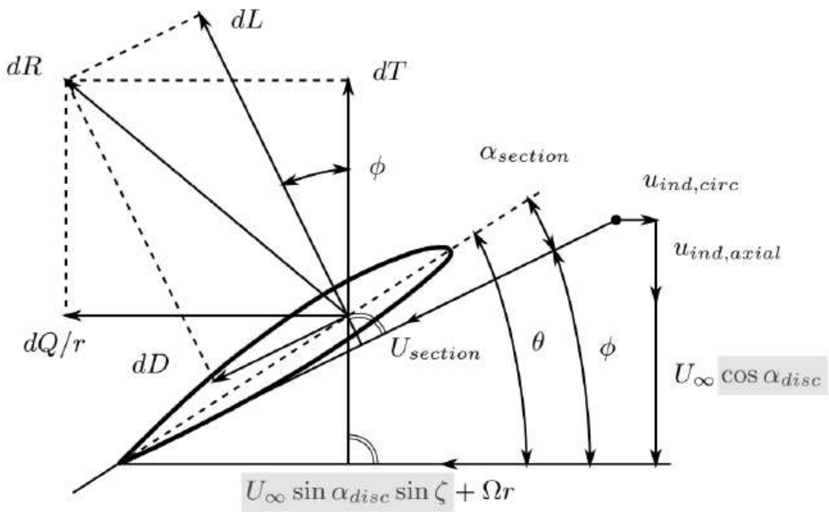

Fig. 2.2: Inflow characteristics at a blade section under non-axial inflow conditions [8]

2.1.2 Characteristical Numbers of Propellers

In this section some parameters are presented that are relevant for the understanding of the aerodynamic loads that will be examined in chapter 6.

Advance Ratio

The advance ratio J is defined as the ratio of the incoming airstream velocity to the simplified tip propeller tip speed

$$J = \frac{U_\infty}{n \cdot D}. \tag{2.1}$$

The inflow angle α_{disc} and the advance ratio J can be transformed to an axial advance ratio κ and a lateral advance ratio μ as shown in fig 2.3 defined as

$$\kappa = J \cdot \cos \alpha_{\mathrm{disc}} = \frac{U_{\mathrm{x}}}{nD} \tag{2.2}$$

$$\mu = J \cdot \sin \alpha_{\mathrm{disc}} = \frac{U_{\mathrm{z}}}{nD}. \tag{2.3}$$

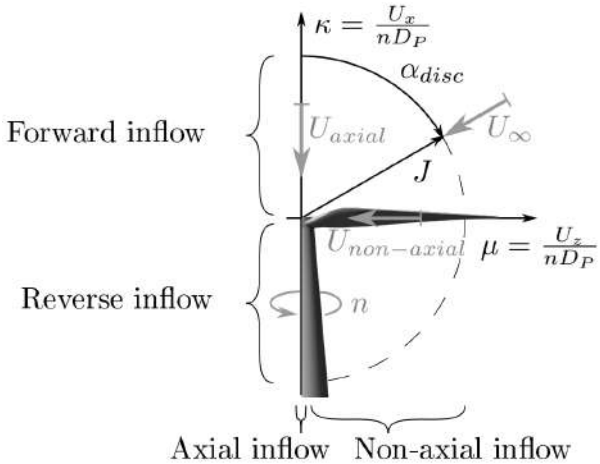

Fig. 2.3: Definition of axial $\boldsymbol{\kappa}$ and lateral advance ratio $\boldsymbol{\mu}$ [8]

Dimensionless Coefficients

To compare the characteristics of different propellers, one normalizes the key figures with the propeller speed, air density and propeller diameter to the following coefficients:

$$c_{\mathrm{F}_{[\mathrm{x,y,z}]}} = \frac{F_{[\mathrm{x,y,z}]}}{\rho n^2 D^4}, \tag{2.4}$$

$$c_{\mathrm{M}_{[\mathrm{x,y,z}]}} = \frac{M_{[\mathrm{x,y,z}]}}{\rho n^2 D^5}, \tag{2.5}$$

$$c_{\mathrm{P}} = \frac{P}{\rho n^3 D^5}. \tag{2.6}$$

In the coordinate system shown in figure 2.1 the force F_{x} corresponds to the thrust T and the moment M_{x} to the needed torque to drive the propeller.
M_{z} represents a yawing torque, whereas M_{y} is a pitching moment always perpendicular to the inflow that for positive values tends to tilt the nacelle upwards.

For the air density the standard value of $\rho = 1.225\,\mathrm{kg/m^3}$ at sea level conditions defined by the International Civil Aviation Organization (ICAO) will be applied [10], as the ALBACOPTER® will fly in low altitudes.

2.1.3 Diameter and Blade Tip Speed

The most important propeller parameter is the diameter of the propeller. This is the decisive parameter for the efficiency of a propeller. From simple momentum considerations it follows that the efficiency of a propeller must increase with increasing diameter. The reason for this is that to achieve a certain change in impulse, which corresponds to the propeller thrust, it is always more efficient to accelerate a large quantity of air a little than to accelerate a small quantity of air a lot, as aerodynamic drag is always proportional to the square of the flow velocity. Consequently propellers should always be as large as possible, but usually there are limiting constraints like the ground clearance [11].

A propeller pitch is always optimized for one specific flight velocity. As eVTOLs with tilting propellers need to be able hover and cruise at high speeds efficiently, which are the most contrary operating conditions, a pitch adjustment mechanism is feasible.

Blade Tip Speed Calculation

For a non-advancing propeller, for example in hover state, the blade tip speed V_{tip} can be calculated with the diameter D and the rotational speed n in s^{-1} by

$$V_{\mathrm{tip}} = \omega \cdot \frac{D}{2} = \pi \cdot D \cdot n \tag{2.7}$$

For a propeller advancing at velocity U_∞ with an inflow angle α_{disc} the resulting tip speed can be calculated by

$$V_{\text{tip}} = \sqrt{(\pi \cdot D \cdot n + \sin \alpha_{\text{disc}} \cdot U_\infty)^2 + (\cos \alpha_{\text{disc}} \cdot U_\infty)^2}. \tag{2.8}$$

When the propeller is tilted into flight direction ($\alpha_{\text{disc}} = 0$) like at a normal airplane, the equation 2.8 simplifies to [12]

$$V_{\text{tip}} = \sqrt{(\pi \cdot D \cdot n)^2 + U_\infty^2}. \tag{2.9}$$

Mach Number Calculation

In general the Mach Number is defined as the ratio of an airspeed U to the speed of sound V_c. In reality the sound velocity depends on several factors like temperature and humidity, but in this work the ICAO standard speed of sound of $V_c = 340\,\mathrm{m\,s^{-1}}$ [10] will be used, because the ALBACOPTER®1.0 will fly in low altitude where it remains almost constant.
The blade tip mach number can be calculated with the blade tip speed as follows:

$$M_{\text{tip}} = \frac{U}{V_c} = \frac{V_{\text{tip}}}{V_c} = \frac{V_{\text{tip}}}{340\,\mathrm{m\,s^{-1}}} \tag{2.10}$$

Maximum Blade Tip Speed

High blade tip speed results in shock waves that increase drag and noise dramatically, lower efficiency and thus increase needed torque. Therefore Gudmundsson recommends not to exceed blade tip mach numbers of 0.75 - 0.8 for composite propellers. [12]

2.1.4 Rotational Inertia

A main problem at scaling up small UAVs is the dynamic behavior of the drivetrain that at large scales can lead to problems. Multicopter drones available today control their flight attitude by changing rapidly the speed of the individual rotors. To change the rotor speed by $10\,\%$, small multicopter drones need less than $10\,\mathrm{ms}$ [13].
However, since the rotational inertia of the rotors increases disproportionately to the diameter, this method cannot be used in the same way for large drones with few rotors. [14]

This can be explained easily if we assume a propeller as a thin rod thin rod with constant mass density and cross-section and and with length $\boldsymbol{l}$. Then its moment of inertia about a perpendicular axis through its center of mass is determined by

$$I_{\mathrm{C}}, rod = \frac{m \cdot l^2}{12}. \tag{2.11}$$

So the moment of inertia depends of a propeller depends on the square of its diameter and its mass, which also depends on the diameter. This has effects on the dynamic behavior of the drive train that cannot be neglected.

The torque $\boldsymbol{M}$ needed to speed up a body with a moment of inertia $\boldsymbol{I}$ with an angular acceleration $\ddot{\varphi}$ is derived by $M = I \cdot \ddot{\varphi}$ [15].

EMAGIC AIRCRAFT admits that the step response of their lifting motors with $15\,\mathrm{kW}$ power and large propellers with a diameter of $2.25\,\mathrm{m}$ is too low for satisfactory flight attitude control [16].

The idea for the ALBACOPTER® 1.0 is to overcome this problem by using a propeller that is able to adjust its pitch very quickly. In this way, the rotational inertia can be used as an advantage for flight attitude control instead of being a disadvantage. If more lift is needed, the propeller just pitches up it's blades some degrees, increases the lift without losing rotational speed because of the inertia and gives the motor time to speed up.

2.1.5 Propeller Efficiency Definition

There are different existing efficiency definitions of propellers, which are presented and discussed in this section.

Tab. 2.1: Different propeller efficiency definitions from [8][17]

Name	Symbol	Formula	Characteristics
"Traditional" propeller efficiency	η_{prop}	$\frac{P_{airflow}}{P_{shaft}} = \frac{U_\infty \cdot T}{2\pi \cdot n \cdot Q} = J \cdot \frac{c_T}{c_P}$	→ Meaningful only for an axial inflow → In hover, the efficiency becomes zero
Power loading	PL	$\frac{T}{P} = \frac{1}{\pi \cdot n \cdot D_P} \cdot \frac{c_T}{c_P}$	→ Closest to intuitive description (shows direct "cost" of propulsion) → Dependent on dimensions
Non-dimensional power loading	c_T/c_P	$n\,D_P\,\frac{T}{P} = \frac{FM}{\sqrt{c_T/2}}$	→ Shows optimal operating point as long as rotational speed and blade tip velocity is kept constant
Figure of Merit	FM	$\frac{P_{ideal}}{P_{real}} = \frac{T \cdot U_i}{\kappa\,P_i + P_0} = \frac{c_T^{3/2}}{\sqrt{2} \cdot c_P}$	→ Shows optimal operating condition as long as diameter is kept constant → Comparison of two FMs of two propellers is only meaningful if disc loading $DL = T/A$ is kept constant
"Traditional" fluid mechanic efficiency	η_{fluid}	$\frac{T \cdot U_\infty}{\dot{m}/2\left(U_{wake}^2 - U_\infty^2\right)} = \frac{\dot{m}\left(U_{wake} - U_\infty\right) \cdot U_\infty}{1/2\,\dot{m}\left(U_{wake}^2 - U_\infty^2\right)} = \frac{2\,U_\infty}{U_{wake} + U_\infty}$	→ Ratio of "useful" propulsive power to the input power, being the change in kinetic energy of the fluid → In hover, the efficiency becomes zero

using

κ	Induced power correction factor	P_0	Profile power
$\dot{m}$	Mass flow through propeller disc	U_i	Induced velocity at propeller disc
P_i	Induced power	U_{wake}	Velocity in the far wake

In table 2.1 numerous definitions for propeller efficiency and their implications are explained.
The traditional propeller efficiency η_{prop} used in literature and propeller calculation software is useful for traditional aircraft. But if the cruise velocity is zero, as in hover state, the efficiency also becomes zero. Therefore in this work the power loading $\boldsymbol{PL}$ will be used for efficiency comparison, as there is only one propeller.

2.1.6 Whirl Flutter

Whirl flutter is an aeroelastic phenomenon that can occur under certain conditions in a motor nacelle with propellers, especially in aircraft with tilting propulsion units. It also occurred in the first tests of the ALBACOPTER® 0.5 propulsion unit. This underlines the importance of the problem, which is why it is explained theoretically here.

The dynamic behavior of an elastically mounted propeller is similar to that of a rigid gyroscope. In the simplest case, the propeller has two tilt eigenmodes for pitch and yaw as shown in figure 2.4 left. In the rotating state these two shapes are coupled by the gyroscopy to two whirl eigenmodes. The higher frequency mode, which is associated to a whirl in direction of propeller direction, is defined as the forward whirl mode [18]. If one also takes into account the air forces on the propeller induced by the gyroscopic oscillations, further couplings arise which can then lead to instability as in figure 2.4 on the down right in the backward whirl mode.

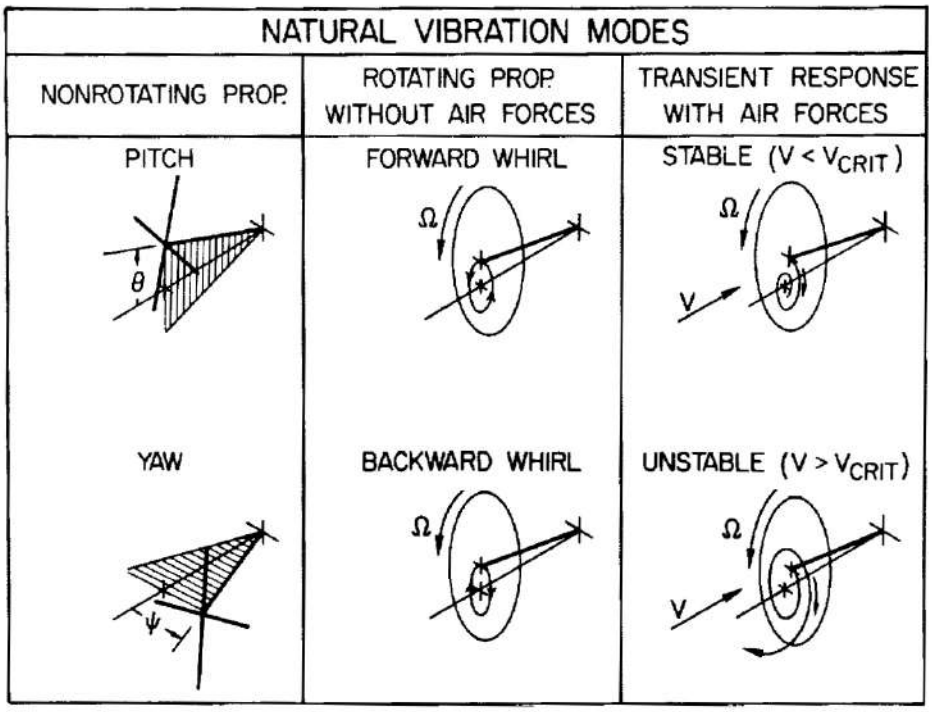

Fig. 2.4: Natural vibration modes of a system with rigid propeller [18]

Decisive for the stability of the system shown in figure 2.4 are, in addition to the inflow conditions (especially advance ratio), above all the clamping stiffnesses. It is widely understood that small restraint stiffnesses, and in particular those of equal pitching and yawing eigenfrequencies, is critical for the stability of the system[19]. Reed also investigated whirl flutter for VTOL aircraft in transition state. He found that non-axial inflow has a stabilizing effect on thrusting propellers. [18]

2.1.7 Blade Element Momentum Theory (BEMT)

The software QBlade is based on BEMT, so the theoretical basis is explained here.

Blade Element Theory (BET) is a widely used method in aerodynamics for analyzing and predicting the performance of rotating wings, such as propellers or wind turbines. It provides a conceptual framework to break down a rotating blade into small sections or elements, and then calculate the aerodynamic forces acting on each element.

The basic principle of Blade Element Theory is to consider each blade element as a separate airfoil, and calculate the forces acting on it based on its local conditions. These forces include lift and drag, which are determined by factors such as the local angle of attack, airfoil characteristics, and the flow conditions around the blade. [12]

One key concept in BET is the notion of induced velocity. As a rotating blade creates lift, it also generates a downward flow of air called downwash. This downwash affects the local angle of attack and modifies the aerodynamic forces on each element. Blade Element Theory takes into account this induced velocity at each element to accurately calculate the forces and performance of the entire blade.

By integrating the forces along the blade span, Blade Element Theory enables the determination of important performance parameters such as thrust, power, efficiency, and torque. These parameters are essential for optimizing the design of propellers and wind turbines, as well as predicting the performance of existing blade systems.

It is important to note that Blade Element Theory has some limitations and simplifications. It assumes steady-state flow, neglects three-dimensional effects, and does not account for complex flow phenomena like flow separation. Therefore, while BET provides valuable insights into the performance of rotating wings, it may not be as accurate as more advanced computational methods for certain flow conditions.[12]

The blade element momentum (BEM) theory is a theory that combines both the blade element theory and the momentum theory. It is used to calculate the local forces on a propeller or wind turbine blade. The blade element theory is combined with the momentum theory to alleviate some of the difficulties in calculating the induced velocities at the rotor.

The blade element momentum theory includes angular momentum in the model, which means that the wake (the air after interacting with the rotor) has angular momentum. That is, the air starts to rotate about the z-axis as soon as it interacts with the rotor.[20]

2.2 Permant Magnet Synchronous Machine (PMSM)

In aviation generally PMSMs are used because they offer the highest power density of all electric motors. Nonetheless, there are different relevant geometries that are presented here. In addition, some criteria for the comparison of electric motors in aviation are discussed.

2.2.1 Motor Geometries

Inrunner PMSM

Inrunner motors are compact and lightweight electric motors where the rotor is located inside the stator. They excel at high rotational speeds and offer excellent efficiency at those speeds. Their compact size and light weight make them suitable for applications with space constraints or weight limitations. As the outer part of the motor stands still, water jacket cooling is possible. Additionally, a very good encapsulation against the environment can be provided. However, they have limited torque output compared to outrunner motors because of the smaller diameter of the airgap.

Outrunner PMSM

Outrunner motors are electric motors where the rotor surrounds the stator. They are known for their higher torque output, making them suitable for applications that require high torque and slower rotational speeds. Because of their large surface area they are usually air-cooled. However, outrunner motors typically operate at lower rotational speeds compared to inrunners and are less efficient at higher speeds. Their larger size can also limit their use in applications with space constraints. Additionally, water cooling is more difficult to realize. The cooling air must be clean, so that no dirt can get into the airgap. [21]

Axial Flux Motors

Axial flux permanent magnet motors have a unique design where the magnetic flux flows parallel to the rotor axis. Rotor and stator a disc-shaped instead of cylindric as shown in figure 2.5. Axial motors are typically shorter and wider than an equivalent radial motor and offer higher power density and torque-to-weight ratio, because they need no yoke, which saves iron mass. The larger surface area of the rotor and stator allows for efficient cooling, making them suitable for high-power applications. [22] Although the design principle is very old, competitive axial flux machines are relatively new [23].

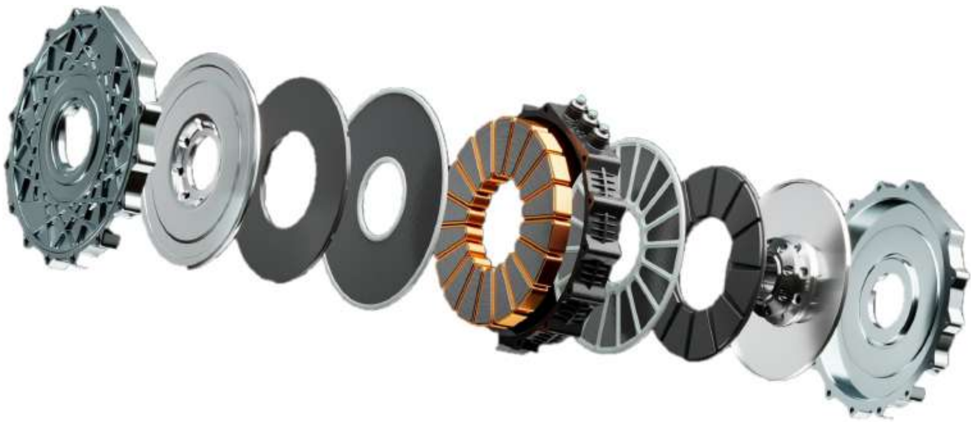

Fig. 2.5: YASA axial flux motor exploded view [23]

2.2.2 Relevant Criteria for Propulsion Systems in Aviation

In aviation, the propeller determines the rotational speed of the propulsion system output shaft, which remains almost constant when compared to a car's drivetrain. In section 2.1.3 is explained how low rotational speeds enhance propeller efficiency. Therefore, achieving higher power and efficiency necessitates a greater torque. For this reason, a continuous torque to weight ratio can be used as a benchmark when comparing electric aircraft motors. Peak torque, given for very short duration, is not relevant for conventional aircraft because they must maintain take-off power for at least one minute. However, peak torque is also essential for eVTOLs because it enables the rapid thrust adjustments needed to control flight attitude.

3 State of the Art of Science and Technology

Based on the fundamental knowledge explained in chapter 2, this chapter gives an overview of the evolution of research on propellers under oblique inflow. Additionally, relevant existing technical solutions for electric drivetrains and eVTOL tilt mechanisms are presented.

3.1 Research on Propellers Under Oblique Inflow Conditions

Propellers facing non-axial inflow have been a field of interest since the very beginning of aviation history in the young twentieth century. A brief overview of the history and current state of research is presented.

McLemore and Cannon [24] at the National Advisory Committee (NACA) investigated a four-blade propeller for inflow angles from $0°$ to $180°$ in 1954 and found that only up to an inflow angle of $15°$ the forces and moments could be predicted analytically. [24] In 1971, Dwyer and McCroskey [25] investigated the three-dimensional flow field in a boundary layer of a helicopter blade to better understand the occurring phenomena. In the field of ship research the problem of predicting the loads of propellers with oblique inflow is also known. In 2011, Amini and Steen [26] conducted model tests on a a 4-bladed azimuth thruster in oblique inflow and used a basic blade element momentum theory to estimate forces and moments.

Also at FRAUNHOFER ICT in the New Drive Systems Department (NAS) research on this topic has been conducted. In his master's thesis, Koleczko [27] developed an analytical method for calculating the flapping moments of propellers with an oblique inflow. It was intended for real-time-calculations for a Hardware-in-the-Loop (HiL) propeller test bench developed at NAS. It is based on the blade element theory and therefore only takes into account the moments resulting from different inflow velocities and angles of attack of the propeller blade sections. Many aerodynamic effects, such as radial flow on propeller blades, are neglected, so the results can only give a rough idea of occurring loads. Also inflow angles higher than 90° are not considered, but need to be investigated for descent and landing.

Recently there have been two works investigating propellers in wind tunnel experiments. Theys et al. [28] used a two-bladed very small propeller for micro aerial vehicles. Cerny [8] analyzed a larger two-blade propeller and provides also unsteady loads from CFD simulation. Therefore his PhD thesis forms an important basis for the present work.

3.2 Electric Drivetrain Topologies in Aviation

While PMSM machines with a fixed-ratio gearbox are typically used in cars, mostly direct drives have been used in aerospace applications to date.

3.2.1 Direct Drives

Several companies offer motors based on different geometries for aviation. GEIGER ENGINEERING offers low-speed air-cooled outrunner motors from $12\,\mathrm{kW}$ to $50\,\mathrm{kW}$ continuous power. They achieve continuous torque densities from $11\,\mathrm{Nm\,kg^{-1}}$ to $15\,\mathrm{Nm\,kg^{-1}}$ and are used in ultralight aircrafts [21].

EMRAX developed various sizes of axial flux motors with continuous torques from $40\,\mathrm{Nm}$ to $500\,\mathrm{Nm}$, dependent of the cooling type (air, water or combined). They are used in many sailplanes. However, their torque densities are smaller than $11.5\,\mathrm{Nm\,kg^{-1}}$ [29].

In 2016, an EXTRA 330LE electric aerobatic plane had it's maiden flight propelled by a motor developed by SIEMENS EAIRCRAFT. It was a water-cooled inrunner with a continuous power of $260\,\mathrm{kW}$ and $1000\,\mathrm{Nm}$ continuous torque at a weight of $50\,\mathrm{kg}$. For the next motor it was intended to increase the continuous torque density up to $30\,\mathrm{Nm\,kg^{-1}}$ [30].

At their production launch, JOBY AVIATION stated that their self-developed dual-wound motor is rated at $236\,\mathrm{kW}$ peak power and $1380\,\mathrm{Nm}$ cont. torque at a weight of $28\,\mathrm{kg}$ including the inverter. It is liquid-cooled and a fan vents the heat exchanger. [3].

It can be concluded that the power and torque density is increased with more powerful motors, but this is true for all machine types. However, most eVTOL manufacturers use large diameter direct drives, including VERTICAL AEROSPACE [31].

3.2.2 Geared Drivetrains

Geared drivetrains are commercially available for RC aircrafts or drones, offered for example by HACKER, but in large aircraft applications they are rare.

ARCHER AVIATION presented a geared drivetrain for their passenger eVTOL that achieves a peak power of $125\,\mathrm{kW}$ weighing $25\,\mathrm{kg}$. The gearbox reduces the rotational speed from $12\,000\,\mathrm{min}^{-1}$ to $2000\,\mathrm{min}^{-1}$ [32].

In 2016, JOBY AVIATION built and tested a geared drivetrain shown in figure 3.1. It is a stepped-planet epicyclic gearbox with sun gear input, fixed carrier and ring gear output. The three planet gears are stepped, i.e. they consist of two gears on a common shaft, to keep the diameter small. Assessing the diameter of the gears as shown in figure 3.1 gives an estimated gear ratio of $i = 14$.

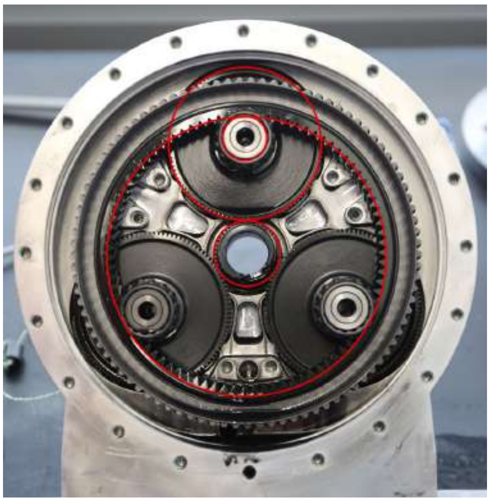

Fig. 3.1: JOBY AVIATION stepped-planet epicyclic gearbox [3]

However, the need for inspections, lubrication, and the resulting vibration led to a switch to direct drive to reduce complexity.

3.3 eVTOL Tilt Mechanisms

The eVTOL manufacturers reveal very little about the tilt actuators of their aircraft.

JOBY AVIATION employs a scissor mechanism that both elevates and tilts the drive forward, resulting in an increased lever arm towards the center of gravity. A rotary actuator moves the mechanism. Both are shown in figure 3.2.

a) b)

Fig. 3.2: a) JOBY AVIATION tilt mechanism and b) tilt actuator unit [3]

On the prototype developed by ARCHER AVIATION, a push rod can be observed that facilitates the tilting of the drive unit around a hinge. Figure 3.3 displays the propulsion unit.

Fig. 3.3: ARCHER AVIATION propulsion unit [32]

4 Regulation and Certification for eVTOLs and Electric Propulsion Systems

The general goal of this chapter is to give an overview about regulations that have to be considered in the design process. No design decisions shall be made that negatively affect the certifiability of the ALBACOPTER® propulsion system. Therefore, first a general overview of existing regulations established by the EUROPEAN UNION AVIATION SAFETY AGENCY (EASA) regarding different classes of eVTOLs is provided and classified with respect to the ALBACOPTER® 1.0. Finally, the relevant regulations for this work regarding electric propulsion systems are summarized.

4.1 Applicable Regulations

The EASA has established different regulations for Unmanned Aerial Vehicles (UAVs) based on their weight class. For each weight class, different rules and requirements apply in terms of registration, training, and operational limitations. The specific details of these regulations can be found in the EASA's "Easy Access Rules for Unmanned Aircraft Systems" (Regulation (EU) 2019/947) [33].
For unmanned cargo drones it is important to know that there is a limitation in maximum take off weight (MTOW) of 600 kg to be in the „specific“ category where the Special Condition Light UAS (SC-LUAS) [34] applies.

So for the entire ALBACOPTER® 1.0 with a MTOW of 800 kg the SC-VTOL presented below will be applicable.

However, as this work deals with a propulsion system that can be scaled and used for different aircraft, there is a Special Condition for electric propulsion systems outlined in section 4.2.

4.1.1 EASA Special Condition for Small-Category VTOL Aircraft

The EASA SC-VTOL [35] is a special condition for the type certification of small-category VTOL aircraft, which are different from conventional rotorcraft or fixed-wing aircraft, and they need a specific set of rules to ensure their safety and performance. The SC-VTOL applies to VTOL aircraft that carry up to nine passengers and have a maximum certified take-off mass of MTOW of $3175\,\mathrm{kg}$ or less.

The EASA SC-VTOL covers various aspects of the design and construction, flight performance, structural loads and strength, occupant protection, fire protection, lightning protection, and lift/thrust system installation of VTOL aircraft. The requirements are further explained in the corresponding Means of Compliance (MOC).

Some of the main requirements are:

- The VTOL aircraft must be able to operate safely in different flight phases, such as hover, transition, and cruise.
- The VTOL aircraft must meet certain standards for flight performance, such as take-off distance, climb rate, stall speed, maximum speed, endurance, range, and landing distance. The VTOL aircraft must also have adequate controllability, stability, and maneuverability in all flight conditions.
- The VTOL aircraft must have a durable structure that can withstand the expected loads and stresses during normal and emergency operations. The VTOL aircraft must also have aeroelastic stability, which means that the structure does not deform or vibrate excessively due to aerodynamic forces.
- The VTOL aircraft must prevent or minimize the risk of fire or explosion due to fuel leakage, electrical faults, or other causes. The VTOL aircraft must also have fire detection and suppression systems in designated fire zones, such as the engine compartment or the lift/thrust system.
- The VTOL aircraft must protect the electrical and electronic systems from damage or malfunction due to lightning strikes. The VTOL aircraft must also have a

lightning protection system that includes shielding, bonding, grounding, surge protection devices, and lightning warning devices.

- The VTOL aircraft must ensure the proper installation and operation of the lift/thrust system components. The VTOL aircraft must also have redundancy and reliability features to prevent or mitigate the loss of lift/thrust.

The EASA SC-VTOL also provides means of compliance (MOC) documents that contain acceptable methods, but not the only methods, of demonstrating compliance with the applicable requirements. The MOC documents include technical specifications, test procedures, analysis methods, design criteria, best practices, and guidance material. For example, the reference volume, in which vertical take-off and landing must be performed, is shown in figure 4.1, with D being about $14\,\mathrm{m}$ for the ALBACOPTER® 1.0.

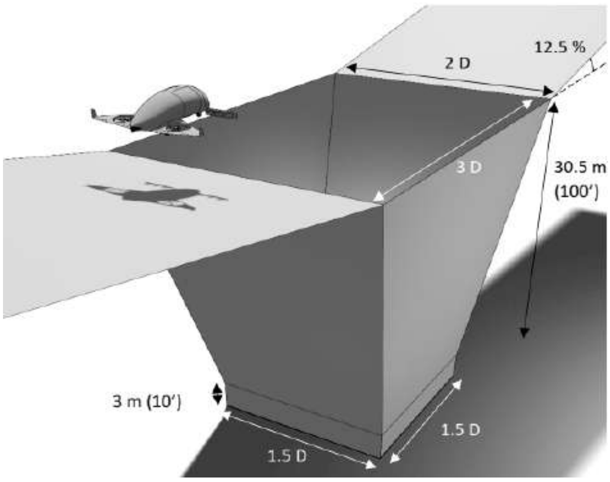

Fig. 4.1: Reference volume for vertical take-off and landing [35]

4.1.2 Special Condition SC E-19 - Electric / Hybrid Propulsion System

The existing certification specifications that are usually applicable are contained in CS-E (engines). For new product architectures such as VTOL the SC E-19 has been developed. The purpose of this special condition is to provide the certification requirements for an Electric and/or Hybrid Propulsion System (EHPS) when the intended aircraft application has already been identified. This Special Condition is applicable to any EHPS, which is used to provide or produce lift or thrust for flight in a manned and unmanned aircraft, during both normal and emergency operations, except for CS-22, CS-LSA, CS-23 Level 1 Day VFR and Light UAS. It should be noted that for CS-25 aircraft, this

Special Condition shall be complemented with appropriate emissions requirements that are yet to be defined for EHPS. [36]

4.2 Summary of Regulation Requirements for ALBACOPTER® 1.0 Propulsion System

The following list is intended to give an overview of the points that are most relevant for the design of the drive system. These are the most important aspects required:

- dedicated manuals with instructions and limitations must be provided
- peak power duration and emergency ratings must be established
- a summary of failure conditions must be made and critical parts identified
- all loads induced by the propulsion system to the aircraft and by the intended aircraft must be specified
- maximum stresses must be determined by tests or validated analysis and not exceed minimum material properties
- A vibration survey must be conducted regarding vibration induced mechanically, aerodynamically, acoustically or by electromagnetic field excitation
- a rotor overspeed must be considered
- windmilling of an inactive propulsion system must not result in unacceptable effects
- enviromental conditions of rain
- a bird or hail strike must not lead to hazardous effects
- recuperation of energy must be considered
- shutdown and restart of the system must be possible in flight
- all applicable propulsion system demonstrations required by the SC E-19 must be performed with a representative propeller.

5 Definition of Further Engineering Constraints and Solution Space

The aim of this chapter is to investigate further limitations that are needed to design the propulsion system. For this purpose, the propeller simulation is presented, the results of which are necessary for the design of the engine and the gearbox. With the resulting rotational speeds the motor and the gearbox can be designed. Finally, some necessary selected external parts are presented.

5.1 Propeller Performance Simulation

To identify achievable thrusts and needed rotational speeds, a simulation of the HELIX H40 propeller is set up. It is also intended to gain a better understanding of the achievable thrust variations by adjusting the blade pitch. To be able to simulate a propeller from a manufacturer that doesn't provide any geometry data, a 3D-scanning process with the corresponding data processing is set up.

5.1.1 Relevant Rotational Speeds for the ALBACOPTER® 1.0

Helix Propeller recommends a rotational speed of $2000\,\mathrm{min}^{-1}$ for their propellers with $1.75\,\mathrm{m}$ diameter for optimal efficiency and a maximum speed of $3400\,\mathrm{min}^{-1}$ is given in the manual [38]. However, the maximum speed is limited by the tested mechanical strength due to centrifugal forces, not for any aerodynamic reason. In normal flight they recommend not to exceed $2400\,\mathrm{min}^{-1}$. An overview of some rotational speeds and their resulting blade tip mach number calculated with equation (2.7) is given in table 5.1.

It shows that in order to prevent trans-sonic shock waves as explained in section 2.1.3 the maximum speed of the propeller should not exceed $3000\,\mathrm{min}^{-1}$.

Tab. 5.1: Rotational velocities and resulting blade tip speeds and mach numbers for ALBACOPTER® 1.0 in hover state

Rotational Speed	Blade Tip Speed	Mach Number
min^{-1}	$\mathrm{m\,s}^{-1}$	
1800	165	0.49
2000	183	0.54
2200	202	0.59
2400	220	0.65
2600	238	0.70
2800	257	0.75
3000	275	0.81

5.1.2 3D-Scanning

As the manufacturer T-MOTOR of the propellers tested for ALBACOPTER® 0.5 doesn't provide any geometry data of the propeller, the geometry can be determined via 3D-Scanning for a later. The objective is to obtain a digital model of the propellers for performance simulation. Therefore a „Shining FreeScan UE Pro“ scanner was used, the scanning process is shown in figure 5.1.

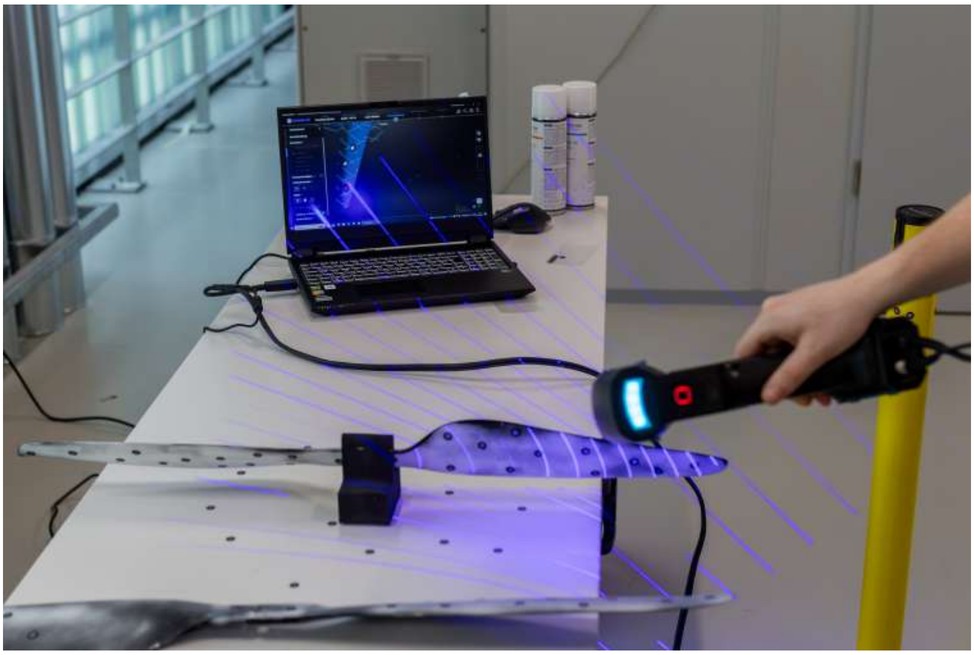

Fig. 5.1: Scanning of the propeller blade

The quality of the retrieved model was better when the table surface was scanned as well and deleted afterwards. This is due to the blades being extremely thin, causing the software to struggle with orienting the upper and lower surfaces to one another.

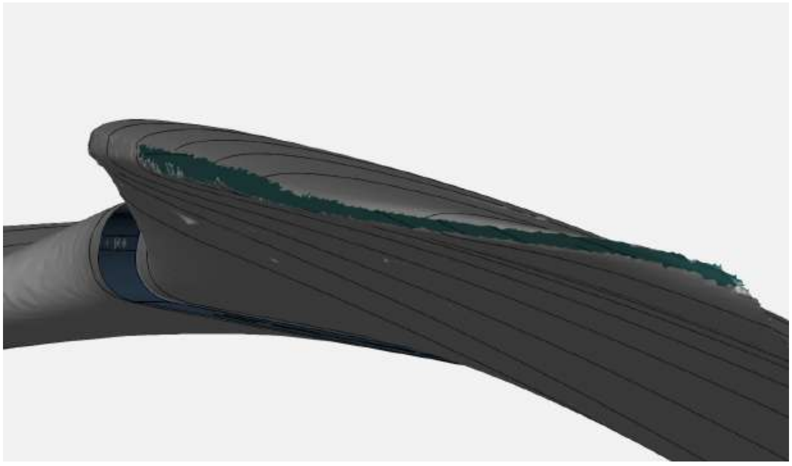

Fig. 5.2: Missing leading edge in the first scan.

In propeller simulation tools a blade is build up by sections with different profiles and associated polars, chord lengths and twist angles. To get this data, the resulting .stl file was oriented into a appropriate coordinate system and several sections were constructed through the geometry. The resulting airfoil data can be exported. In general, the scanner's resolution is high enough to produce more than five times points per section than necesssary (and usable) per section. However, the leading and trailing edge of the blade are not always captured correctly as illustrated in figure 5.2. Therefore it can be necessary to reshape the profile with splines to get smooth profiles, using for example XFLR 5[39] as shown in figure 5.3. The resulting profile data can be used in various propeller analysis tools.

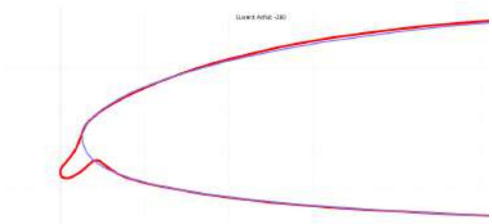

Fig. 5.3: Scanned faulty leading edge and reshaped airfoil

5.1.3 Simulation Methodology

For the propeller performance simulation of the propeller intended for the ALBACOPTER® 1.0 the free software QBLADE was used. A quick overview of the preprocessing is given here, for further details on theory refer to the QBLADE documentation [20].

From the blade CAD model provided by HELIX the needed geometry data could be extracted. These are the chord length and twist angle distribution and the airfoils. The airfoils were extracted by exporting 200 points per cross-section cut. The airfoils are analyzed by making use of XFOIL which calculates the pressure distribution of the airfoils and hence the lift and drag polars. For this step a Mach and Reynolds Number are needed, which are calculated in table 5.2. In the next module, the polars need to be extrapolated using Montgomerie (or Viterna) method to an angle of attack range from $-180°$ to $180°$. Finally the propeller blades are defined by assigning the geometry data and airfoil polars to the different sections of the blade. Then an analysis of the propeller performance can be conducted with the application of tip loss and 3D correction factors.

Fig. 5.4: Propeller Blade Design in QBLADE

Tab. 5.2: Input Data for Propeller Simulation for rotational speed of $2000\,\mathrm{min}^{-1}$

radial station mm	chord mm	twist angle °	section velocity $\mathrm{m\,s^{-1}}$	Mach Number	Reynolds Number
200	86.00	40.86	41.89	0.12	257 311
425	87.00	25.2	89.01	0.26	553 144
572.5	81.18	19.13	119.90	0.35	695 276
651	75.00	16.6	136.35	0.40	730 420
792.5	53.34	13.15	165.98	0.49	632 415
837.2	40.19	11.91	175.34	0.52	503 320
870	16.40	10.14	182.21	0.54	213 448

5.1.4 Simulation Results

In this section, the results of the propeller performance simulation are presented and explained.

In figure 5.5 the hover thrust over the required power is plotted for different rotational speeds. Every point represent a blade pitch angle variation of $1°$ from $-14°$ to$16°$. As defined in table 2.1, in hover the thrust to power ratio is used as efficiency measure. It can be seen that every rotational speed has it's maximum thrust, which can only be surpassed by a small amount at a much higher power consumption and thus very low efficiency. At $2000\,\mathrm{min}^{-1}$, which is the manufacturer's recommended speed as mentionend in section 5.1.1, the maximum reasonable thrust achievable is approximately $1000\,\mathrm{N}$, which is sufficient for hover. With $2400\,\mathrm{min}^{-1}$ $1400\,\mathrm{N}$ of hover thrust can be reached, whereas with the pre-defined maximum power of $50\,\mathrm{kW}$ about $2000\,\mathrm{N}$ of thrust could be produced.

Taking a closer look at the same graphs for the hover situation depicted in figure 5.6, which in theory would require $981\,\mathrm{N}$ of thrust as each of the 8 rotors has to carry $100\,\mathrm{kg}$, it becomes clear that a rotational speed of $2000\,\mathrm{min}^{-1}$ may be insufficient for hover and $2200\,\mathrm{min}^{-1}$ could be a more optimal choice. In addition, $2200\,\mathrm{min}^{-1}$ also may provide sufficient reserves for a fast blade pitch adjustment for flight attitude control. Nonetheless, these findings require further investigation on a test bench.

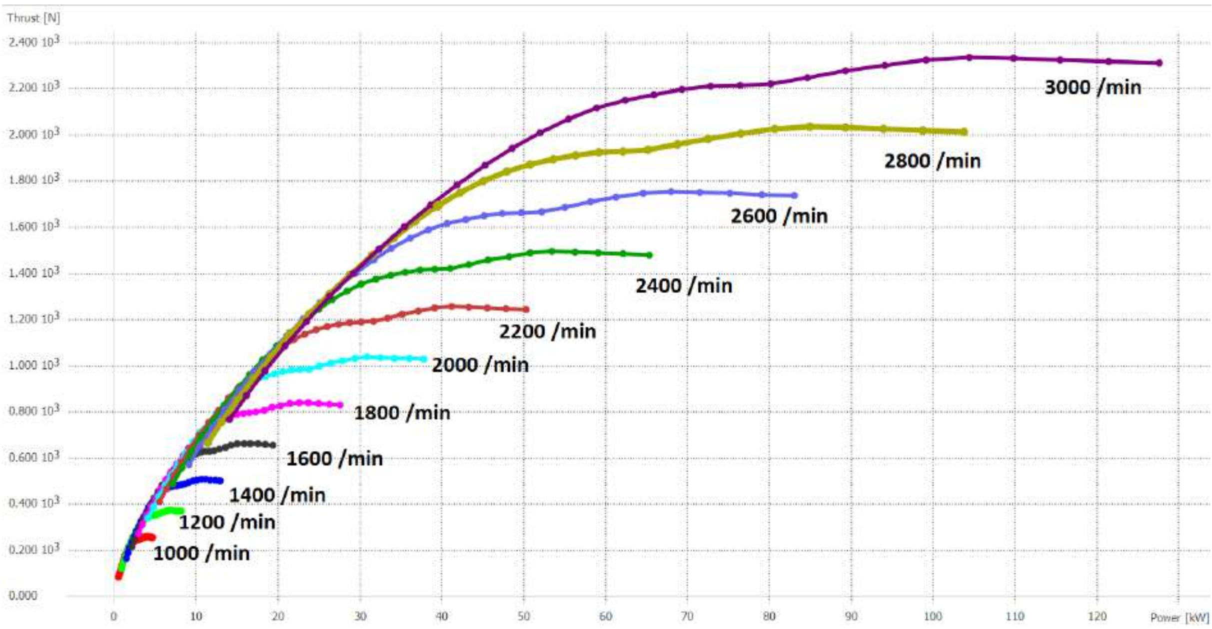

Fig. 5.5: Thrust over power for different rotational speeds

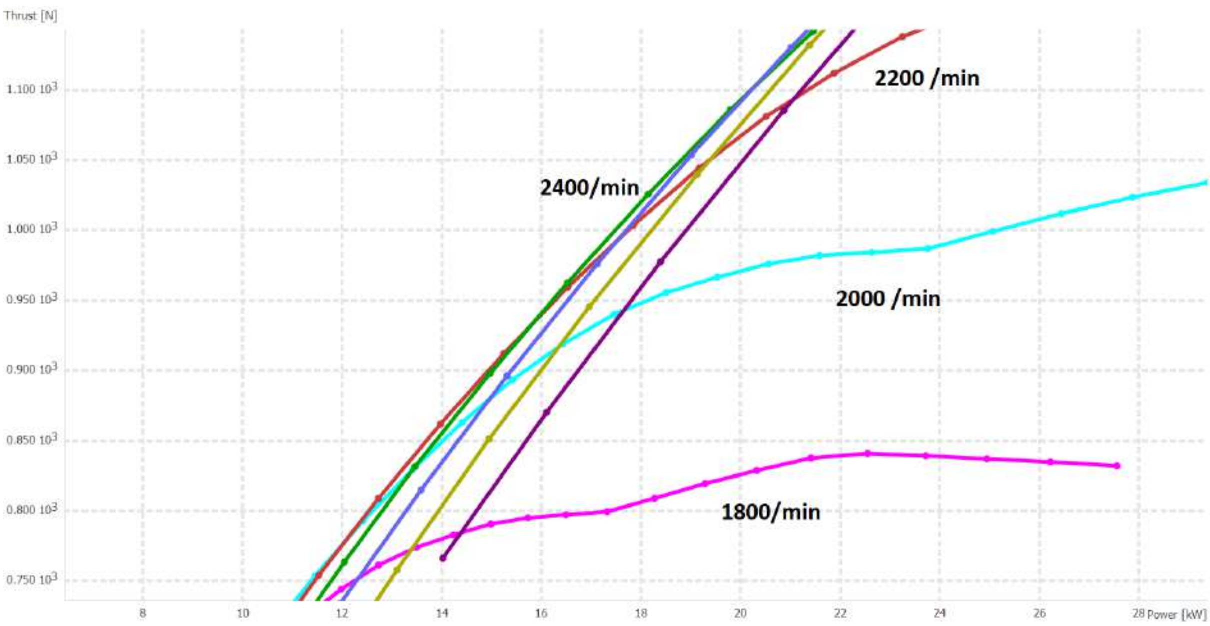

Fig. 5.6: Thrust around hover thrust over power for different blade pitches

5.2 Definition of Key Performance Values of the Drivetrain

After defining the propeller's characteristics, it is essential to know the key performance data of the motor to be able to make a preliminary gear design. To maximize the advantage of the high-speed drivetrain concept, the motor must be operated at the highest possible speeds with a high reduction gear ratio to achieve the lowest possible weight for a given power output.

5.2.1 Electric Motor and Inverter

The LOI project partner SciMo develops a customized motor for the Albacopter® 1.0 which is presented here. It is an inrunner permanent magnet synchronous machine with water jacket cooling. The rotor features the same cooling circuit to make use of one pump. To achieve a higher level of integration and a lightweight design, the bearing shield of the output side will also be one part of the gear housing as shown in figure 5.8 and contain also a cooling water channel. The most important data is given in table 5.3, the complete data sheet can be found in appendix C.

Tab. 5.3: Preliminary specifications of the SciMo SY32

Continuous Power	34	kW
Maximum Power	60	kW
Estimated Weight	6	kg
Peak Torque	23	Nm
Maximum Speed	30 000	min^{-1}

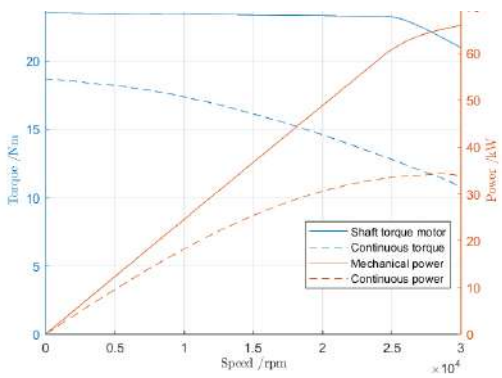

Fig. 5.7: Torque and power diagram for SY32

In figure 5.7 the output torque and power are plotted as peak and continuous values over the motor speed. However, it is important to know that the peak power will be available only for some seconds, up to half a minute when started at cold state due to the cooling of the inverter.

To operate the motor, SCIMO has developed a corresponding inverter utilizing silicon carbide technology for up to $750\,\mathrm{V}$ DC link voltage. Additionally, a small controller board is required to establish a connection between the system and the aircraft's CAN bus system. This serves as the drive unit.Due to its intended compact and lightweight design, the controller and inverter are affixed to the motor. A shared cooling system is a practical choice, as the inverter also requires water-cooling.

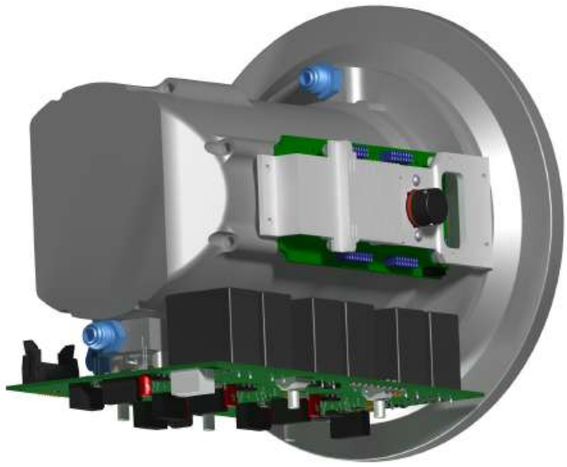

Fig. 5.8: SCIMO SY32 motor assembly with inverter and controller board

5.2.2 Gear Ratio and Possible Gear Types

To maximize the benefit of the high-speed drivetrain concept, a high gear ratio is needed. As mentioned in section 5.1.1, the typical rotational speed of the propeller is $2000\,\mathrm{min}^{-1}$ and in section 5.1.4 it is shown that the propeller is able to produce sufficient thrust for hover at this speed.

SCIMO gives a rotational speed of $25\,000\,\mathrm{min}^{-1}$ for continuous power. The ratio of the two speeds leads to a gear ratio of $i = 12.5$. However, with this high gear ratio the propeller speed is limited to $30\,000\,\mathrm{min}^{-1}/12.5 = 2400\,\mathrm{min}^{-1}$ under normal operating conditions.

The determined gear reduction ratio of 12.5 can be achieved reasonably either by a spur gear or a planetary gear.

A spur gear unit is very simple and common, but needs two stages to achieve this reduction ratio without getting too large.

A planetary gear can achieve the required reduction ratio a single stage, and has high efficiency and load capacity. In addition it has a circular cross-section like the electric motor, but would have a larger diameter. Another advantage is the absence of bearing loads due to the axial symmetry. However, planetary gears are more complex and expensive in comparison to spur gears. High rotational speeds of the planet gears can also lead to problems due to centrifugal forces.

5.3 Peripheral Components

5.3.1 Cooling System

The SciMo SY32 motor is rated with a coolant flow rate of $6\,\mathrm{L\,min^{-1}}$ and an inlet temperature of $65\,°\mathrm{C}$. As the cooling circuit combines the cooling of the inverter, the rotor and water jacket for the stator in series, a pressure drop of more than $1\,\mathrm{bar}$ is assumed.

Coolant Pump

Sobek Motorsport provides a redundant but lightweight pump for aircraft applications. It features two BLDC motors and two power controllers, which and is shown in figure 5.9. It can be connected to the CAN bus system and pump and more than $10\,\mathrm{L\,min^{-1}}$ at a pressure difference of $1.6\,\mathrm{bar}$. As a working cooling system is essential for the electric motors and a fault can pose serious danger to the aircraft, a small additional weight to a total of $370\,\mathrm{g}$ is acceptable.

Fig. 5.9: Sobek Z-P 2200

Heat Exchanger

The ideal geometry for a water cooler would be circular, aligning with the motor geometry. However, achieving this circular geometry is only possible with flat tube heat exchangers, but would be expensive for a prototype due to the associated tooling costs. Despite this, the Plate Fin Heat Exchanger has become the preferred option for aviation applications due to its corrosion resistance; however, it can only be designed in rectangular shapes. [40] The corrosion resistance results from the manufacturing process known as Controlled Atmosphere Brazing (CAB), which operates through tight tolerances without flux, a component that would drastically reduce corrosion resistance.

5.3.2 Slip Ring

The stepper motor housed in the propeller hub for blade pitch adjustment requires a power supply. Thus, the gear's output shaft must be made hollow to house the cables. To transfer the electric power from the non-rotating portion to the propeller hub, a slip ring is necessary. In a spur gear design the slip ring can be placed within the hollow output shaft to achieve a compact packaging and encapsulation. However, in a planetary gear concept this is not possible, as planets rotate around the shaft inside the planetary gear. So, some type of hollow shaft slip ring is necessary.

MT-Propeller [41] produces customized pancake slip rings for their electrically controlled constant speed propeller. However, a commercially available slip ring will be used for the intended propulsion system. There are hollow-shaft slip rings available that can sustain high rotational speeds. The GT38109 from MOFLON (figure 5.10) was selected and can be ordered with various numbers of rings [22].It has a inner diameter of $38\,\mathrm{mm}$ and an outer diameter of $109\,\mathrm{mm}$. To fit a smaller output shaft diameter, a small sleeve can be added.

Fig. 5.10: MOFLON GT38109 hollow-shaft slip ring [42]

6 Investigation of Loads on Tilted Rotors

In order to design the drive system correctly, it is of elementary importance to determine all possible loads that may occur. Therefore, in this chapter first the steady and unsteady aerodynamic loads resulting from non-axial inflow are calculated. Then the results and other possible design loads are considered and evaluated.

6.1 Extrapolation of Aerodynamic Loads from Literature Data

Cerny investigated in his PhD thesis [8] the effects of non-axial inflow on the aerodynamic characteristics of propellers. He analyzed a two-blade small-scale fixed-pitch propeller in the wind tunnel, measuring the loads and capturing the flow field with Particle Image Velocimetry (PIV), and with CFD simulations.

Propeller Geometry Comparison

As long as the geometry and the Reynolds number are similar, propellers of different sizes and rotational speed can be compared by dimensionless coefficients.Therefore the relative geometry (chord length divided by propeller radius and the tilt angle) will be compared in this section.

In figure 6.1 the difference in shape and size of the HELIX H40 L-TM intended to be used for the Albacopter® 1.0 and the 18 inch propeller investigated by Cerny get clear. The APC 18x8E is a thin propeller made of fiberglass composite for model aircraft, whereas the Helix propeller, with almost four times the diameter, is made of carbon fiber composite and can also be used with combustion engines [38], which have higher vibration characteristics [43]. It has a much thicker profile in the inner section in comparison to the APC 18x8E propeller, which uses a highly cambered Eppler E-63 with $16.89\,\%$ relative thickness near the hub [44].

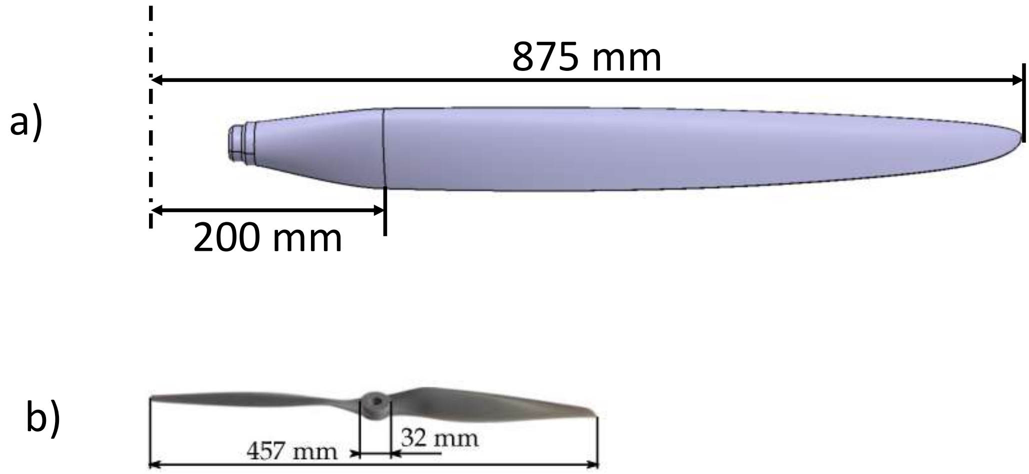

Fig. 6.1: Size comparison between a) Helix H40 L-TM propeller and b) APC 18x8E propeller analyzed by Cerny[8]

The relative chord length of the two propellers, shown in figure 6.2, are different, especially in the inner part, but at $0.75\,\mathrm{r/R}$ (relative radius), which is the typical reference radius for manufacturers [12], they are almost the same.

The twist angle distribution is pretty similar, but contains a rather constant offset becoming smaller at the blade's fin. As the propeller's pitch will be variable, the given similar course of the twist angle is satisfying.

Cerny ran the propeller for the tests with a rotational velocity of $4000\,\mathrm{min}^{-1}$. Based on the local chord length c the local Reynolds numbers range between $4 \cdot 10^4$ and $12 \cdot 10^4$ using $Re(r) = 2\pi \cdot r \cdot n \cdot c(r)/\nu$.[8] For the HELIX H40 propeller running at $2000\,\mathrm{min}^{-1}$ the local Reynolds numbers range between $20 \cdot 10^4$ and $75 \cdot 10^4$ and at $2400\,\mathrm{min}^{-1}$ the Reynolds number can exceed $90 \cdot 10^4$.

Nonetheless, as this is the most recent and extensive investigation, the database will be used for the load estimation.

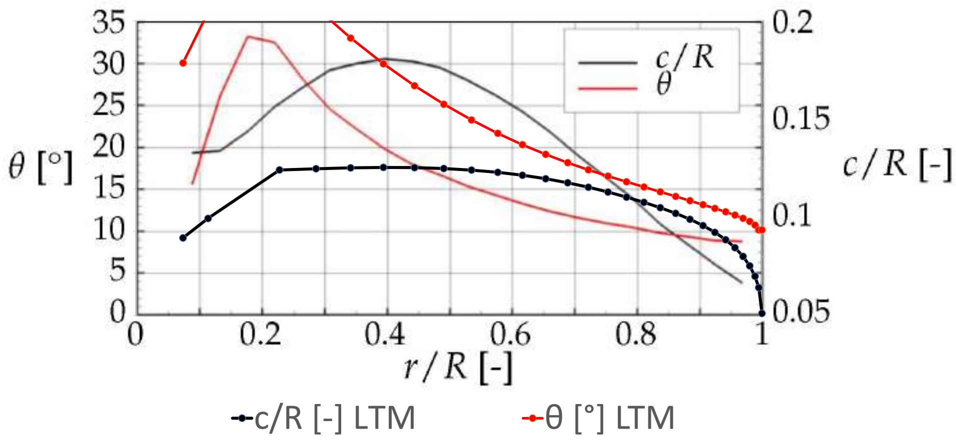

Fig. 6.2: Comparison of blade chord length and twist angle between Helix LTM Propeller (dotted lines) and APC 18x8E

6.1.1 Extrapolation of Static Loads from Wind Tunnel Experiment Data

The wind tunnel test setup is shown in figure 6.3. The propeller and the speed-controlled motor was connected to a six-component internal balance. The whole system was rotated in the wind tunnel to obtain the aerodynamic loads at inflow angles from $\alpha_{\text{disc}} = 0°$ to $180°$. All load measurements from wind tunnel data are averaged over $30\,\text{s}$ [8].

The resulting loads are illustrated by contour plots over the axial advance ratio κ and the lateral advance ratio μ (see figure 2.3). In these plots, the distance from the origin represents the magnitude of the propeller advance ratio J.

As the transition phase, where non-axial inflow will occur, ends with the beginning of the climb phase (see section 1.4), the maximum regarded advance ration is defined by the horizontal climb speed of the ALBACOPTER® 1.0. The estimated horizontal climb speed of $32\,\text{m}\,\text{s}^{-1}$ thrusted by a propeller with a diameter of $1.75\,\text{m}$ and rotational speed $n = 2200\,\text{min}^{-1} = 40\,\text{s}^{-1}$ ($10\,\%$ above recommended speed) corresponds to an advance ratio of $J = 0.5$.

Therefore, the maximum load coefficients are searched within a half circle with radius of 0.5 representing the area with this advance ratio and every possible inflow angle. Their magnitude is determined optically, as it was not possible to get access to the data.

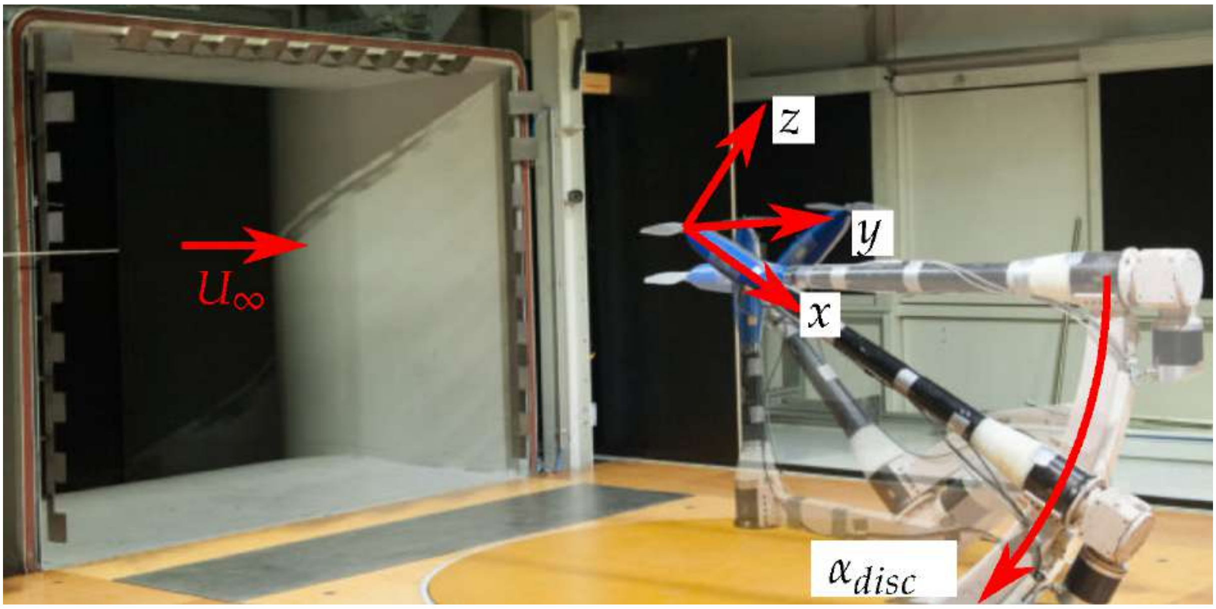

Fig. 6.3: Wind tunnel setup used by Cerny[8]

The resulting contour plot for the yawing moment (around z-axis) $c_\mathrm{n} = c_{\mathrm{M_z}}$ and pitching (tilting) moment $c_\mathrm{m} = c_{\mathrm{M_y}}$ coefficient, which represents a moment around the y-axis, are shown in figure 6.4. Within $J = 0.5$, the yawing moment shows primarily a dependency of the lateral advance ratio. This is expected, as a the airspeed difference between advancing and retreating propeller blade increase with lateral velocity. The highest value of 0.008 is achieved for a lateral advance ratio larger than 0.4.

The situation for the pitching moment, represented by the coefficient c_m, is different. Calculating this moment with analytical methods predicts only a time-dependent moment, but no average value (see [27]). Only numerical methods of higher fidelity are able to predict a mean moment. Its maximum value in the total by Cerny investigated area is six times smaller than c_n, but it appears also within the area relevant for ALBACOPTER® 1.0.

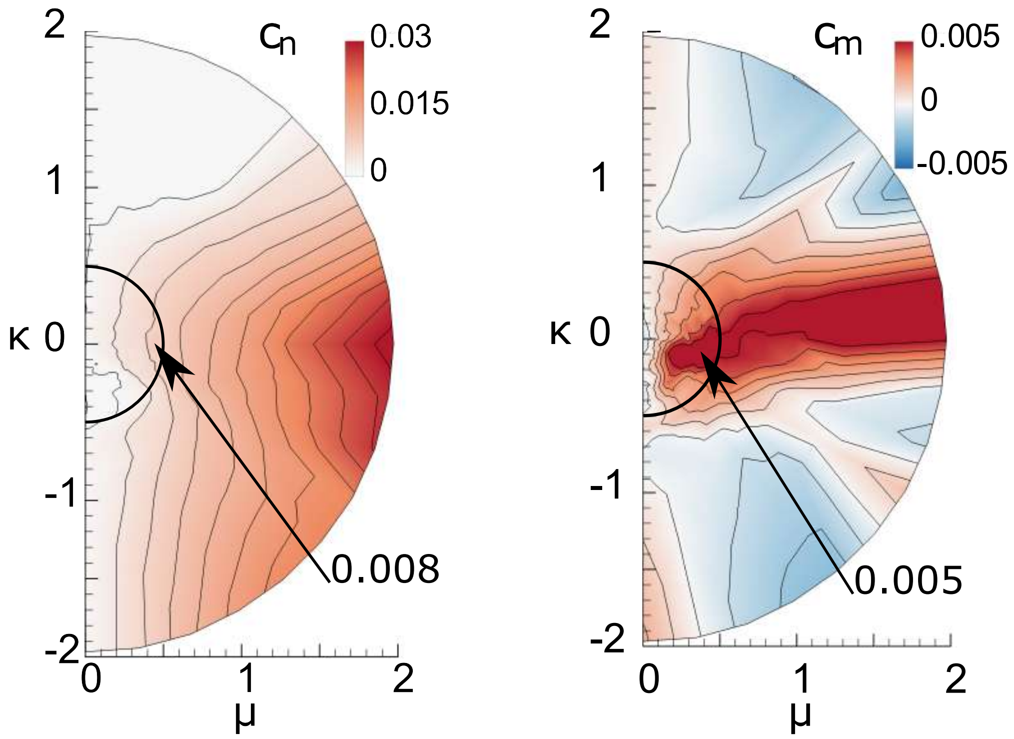

Yawing Moment coefficient $c_{\mathrm{n}} = c_{\mathrm{M_z}}$ Pitching Moment coefficient $c_{\mathrm{m}} = c_{\mathrm{M_y}}$

Fig. 6.4: Resulting yawing (left) and pitching/tilting (right) moment coefficient contour plots with estimated maximum coefficients within $J = 0.5$

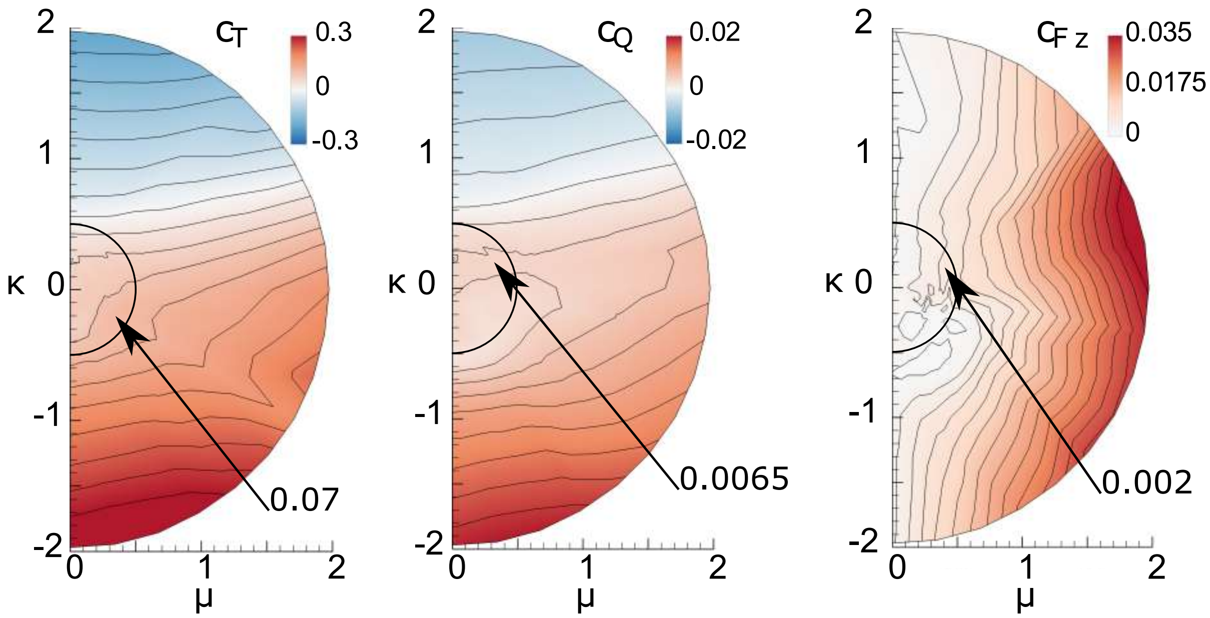

Thrust coefficient Torque coefficient Upward (z) force coefficient

Fig. 6.5: Resulting contour plots with maximum coefficients within $J = 0.5$

In figure 6.5 the coefficient maps for thrust, upward side force (in z direction), and torque are plotted. The thrust coefficient and torque display a similar behavior, with the axial advance ratio μ being the primary influence. This effect can also be shown with a conventional BEMT propeller simulation. When the axial advance ration gets too high, the propeller stops thrusting and starts windmilling, which can be recognized by negative coefficients. The side force coefficient is primarily dependent on the the lateral advance ratio μ. However, the coefficient within the field of interest is almost negligible.

Table 6.1 summarizes the obtained maximum coefficients and the respective load strengths at a rotational velocity of $2400\,\mathrm{min}^{-1}$. The strengths are calculated using the equations given in section 2.1.2.

Tab. 6.1: Maximum Steady Force Coefficients and Strength Values for ALBACOPTER® 1.0 at $J = 0.5$ at $2400\,\mathrm{min}^{-1}$

Load	**max. coeff.**	**Strength**
Thrust T	0.07	$1287\,\mathrm{N}$
Upward Force F_{Z}	0.002	$37\,\mathrm{N}$
Torque	0.0065	$209\,\mathrm{Nm}$
Power	0.041	$53\,\mathrm{kW}$
Pitching Moment M_{Y}	0.005	$161\,\mathrm{Nm}$
Yawing Moment M_{Z}	0.008	$257\,\mathrm{Nm}$

6.1.2 Extrapolation of Unsteady Loads from CFD Simulation Data

> „The occurring unsteady loads of a propeller system are of elementary importance for its design process to determine the loads on the propeller shaft, the bearings, and to gain information concerning correlated vibrations.“ Cerny [8]

Cerny et al. [45] compared different numerical approaches to calculate the occurring loads and concluded that unsteady Reynolds-averaged Navier-Stokes-Calculations URANS showed the best agreement with experimental results.

An inflow velocity of $23\,\mathrm{m\,s^{-1}}$, which represents the drone's maximum estimated stall speed in wingborne flight, driven by a propeller with a diameter of $1.75\,\mathrm{m}$ and rotational speed $n = 2400\,\mathrm{min}^{-1} = 40\,\mathrm{s}^{-1}$ corresponds to an advance ratio $\boldsymbol{J} = 0.33$.

In figure 6.6 the loads in all directions are plotted for the inflow angles $\alpha_{\mathrm{disc}} = 30°, 60°$ and $120°$ over one propeller revolution. All load curves contain generally two repetitions due to the two-bladed propeller. In the sketch above the loads at the sections $r/R = 0.75$ are illustrated for a inflow vector shown on the left.

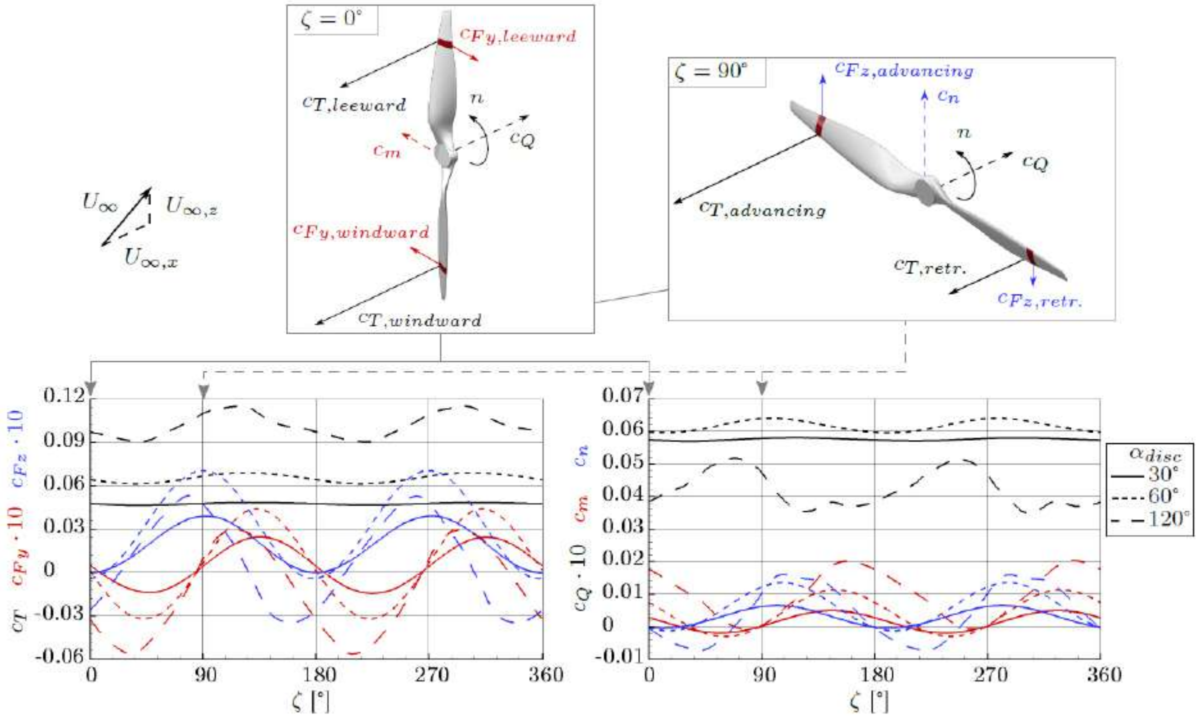

Fig. 6.6: Time-resolved force (left) and moment coefficients (right) over one propeller revolution at $J = 0.33$ [8]

Tab. 6.2: Maximum Transient Force Coefficients and Strength Values for ALBACOPTER® 1.0 at $J = 0.33$ and $2400\,\mathrm{min}^{-1}$

Inflow Angle	**Thrust**		**Lateral Side Force**		**Upward Force**	
α_{disc}	c_{T}	$T = F_{\mathrm{X}}$ /N	$c_{\mathrm{F_Y}}$	F_{Y} /N	$c_{\mathrm{F_Z}}$	F_{Z} /N
60°	0.07	1287	0.005	92	0.007	129
120°	0.115	2114	0.006	110	0.0054	99

Table 6.2 summarizes the obtained maximum coefficients and the respective forces at a rotational velocity of $2400\,\mathrm{min}^{-1}$. It's worth noting that the mean thrust coefficient for $\alpha_{\mathrm{disc}} = 120°$ from this diagram is significant larger than in the contour plots, although the advance ratio is smaller. The same observation can be made for the mean value of the pitching moment coefficient, whereas the the mean yawing moment coefficient corresponds to the experimental result. All maximum moment coefficients are displayed in table 6.3 .

Tab. 6.3: Maximum Moment Coefficients and Strength Values for ALBACOPTER® 1.0 at $J = 0.33$ and $2400\,\mathrm{min}^{-1}$

Inflow Angle	**Torque**		**Power**	**Pitching Moment**		**Yawing Moment**	
α_{disc}	$c_{\mathrm{Q}} = c_{\mathrm{M_X}}$	T /Nm	P/kW	$c_{\mathrm{M_Y}} = c_{\mathrm{m}}$	M_{Y} /Nm	$c_{\mathrm{M_Z}} = c_{\mathrm{n}}$	M_{Z} /Nm
60°	0.0065	209	53	0.012	386	0.014	450
120°	0.0054	174	44	0.02	643	0.016	515

6.2 Comparison with Internal Wind Tunnel Experiments

With a boom and two drive units of the ALBACOPTER® 0.5, tests were carried out in the wind tunnel of the University of Dresden with different inflow velocities and three different propellers at different speeds. In each case, both drives were tilted from the horizontal position to the vertical position and back again simultaneously. The complete setup is shown in figure 6.7. The drivetrain is tilted by an industrial servo actuator connected to a ball screw.

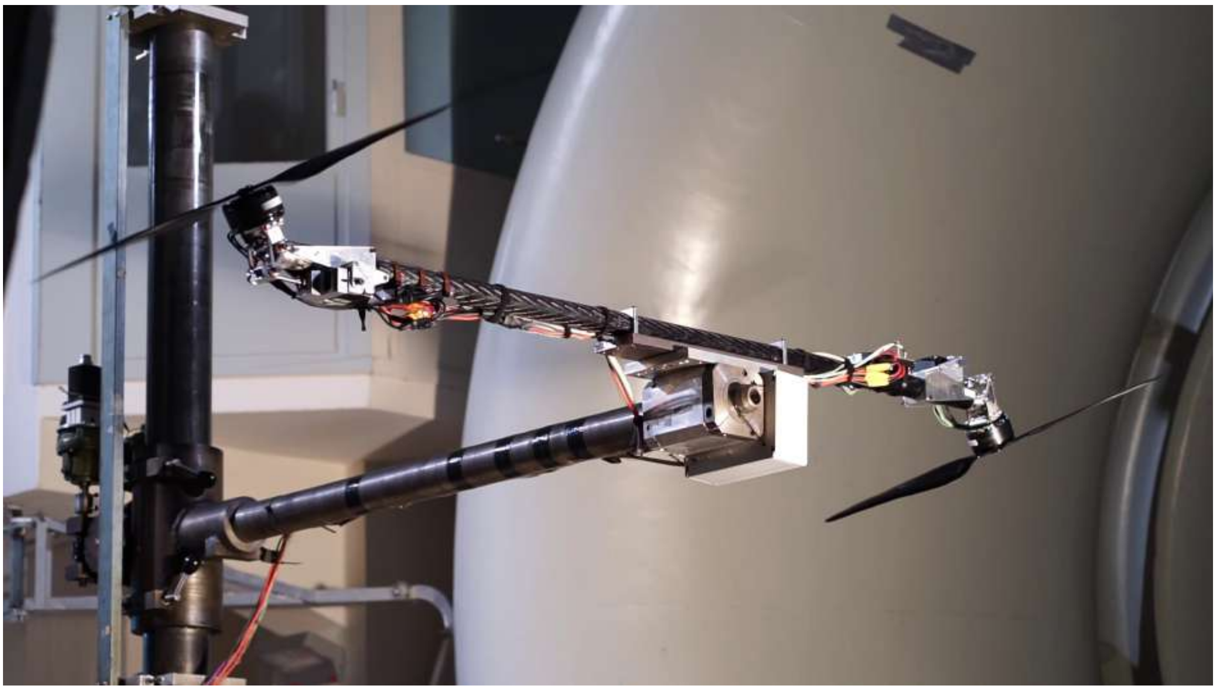

Fig. 6.7: ALBACOPTER® 0.5 wind tunnel test setup

Unfortunately the six-component balance failed, so no loads could be measured. But the servo motor's current and tilt angle got logged and can be used for a tilting moment estimation.

Figure 6.8 shows an example of the course of the tilt angle and the actuator current in a wind tunnel test with the T-motor 32-inch propeller at 4000 rpm and $100\,\mathrm{km\,h^{-1}}$ wind speed in the channel.

Unfortunately, the actuator current's course is very noisy. Smoothing the noise throughout the entire course is ineffective due to the current steps when the actuator starts and stops tilting. However, it is still possible to estimate an approximate course.

Since the voltage and tilt speed are approximately constant, the actuator current is roughly proportional to the tilt moment. This is can be explained with the power equation $M = P/(2\pi \cdot n \cdot \eta)$ with $P = U \cdot I$, but the efficiency of the actuator system cannot be assumed as constant. Hence, it only gives a rough overview. For reference, the plots of all conducted experiments can be found in the appendix in appendix A.1.

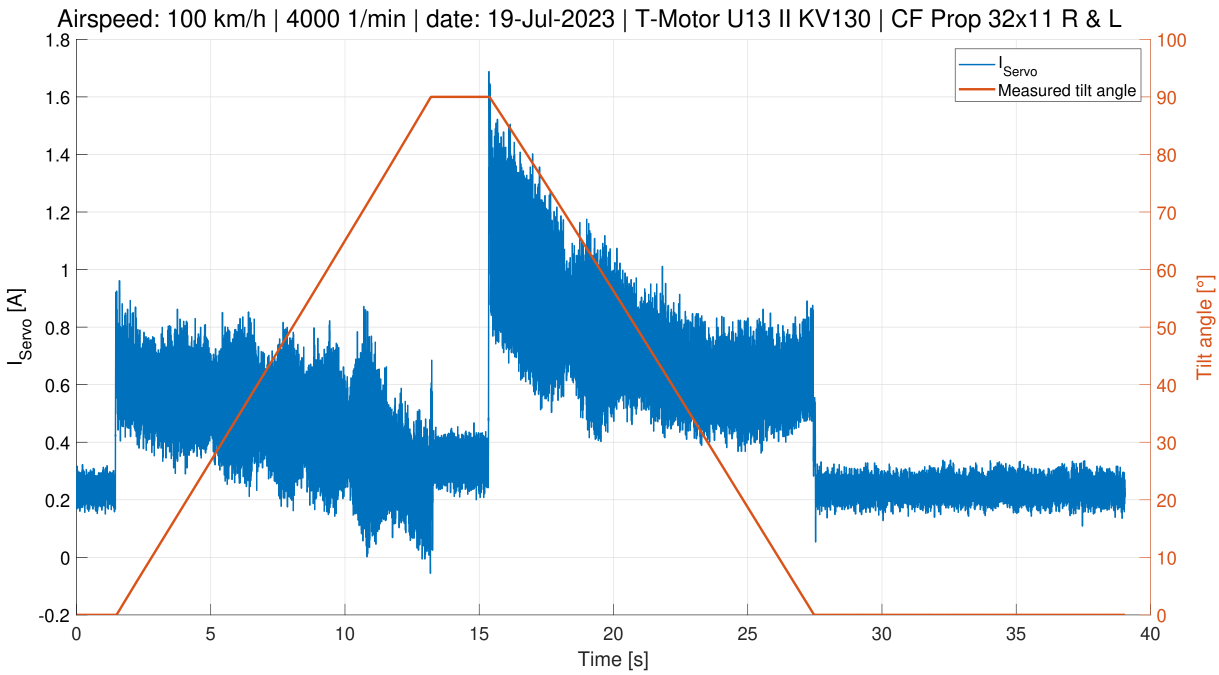

Fig. 6.8: Tilt 0°-90°-0° and actuator current at $100\,\mathrm{km\,h^{-1}}$ with 32 inch propeller at $4000\,\mathrm{min^{-1}}$

When the drive is tilted up, the current decreases as the tilt angle increases. When tilting back down from the 90° position in the direction of flow, most current is required initially and then progressively less, but generally more than when tilting up. These two observations indicate an aerodynamic moment that causes the propeller hub to tilt up and is largest when the inflow is completely lateral. These two observations are consistent with the contour plot from the work of Cerny [8].

The test was conducted with a diameter, rotational speed, and inflow velocity that resulted in an advance ratio of $\boldsymbol{J} = v_\infty / n \cdot D$ of 0.5, so the tilt means a travel back and forth along a quarter circle arc with radius 0.5 through the pitching moment contour plot as shown in figure 6.9. The course of the moment coefficient is approximately linear with the tilt angle, and the course of the actuator current in fig. 6.8 is almost likewise during the tilting phases. Above $70°$ in both diagrams an steeper increase in actuator current, respectively tilting moment, can be observed.

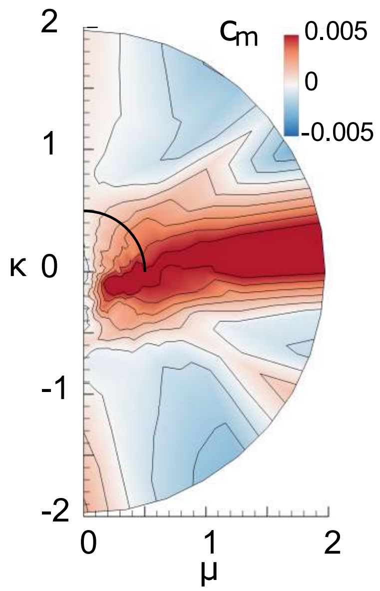

Fig. 6.9: Tilt $0°$ - $90°$ - $0°$ (represented by black arc) at $100\,\mathrm{km\,h^{-1}}$ with 32 inch propeller at $4000\,\mathrm{min^{-1}}$ in tilt moment coefficient diagram from Cerny[8]

However, the servo actuator must overcome more than aerodynamic loads. It also faces friction losses and inertias, or gyroscopic forces. The friction losses can only be estimated on average. Especially during start-up, the higher static friction in the ball screw is expected to contribute significantly to the actuator current peaks.

6.3 Design Loads for ALBACOPTER® 1.0

6.3.1 Emergency Situations Consideration

As shown in section 4.2, EASA regulations require peak power duration and emergency ratings. A very common scenario is called One Engine Inoperative (OEI), so that the remaining propulsion unit must provide the necessary thrust. There are different ratings for multi-engine aircraft regarding the duration of the OEI power, from 30 seconds to continuous. In any case, it is important to consider the failure of one or even more drive systems. It is not clear whether, in the event of failure of one propulsion system, the opposite one would also have to be switched off in order to be able to maintain stability around the vertical axis during hovering. The worst time for a drive failure of the ALBACOPTER® 1.0 would be at the end of the transition, which according to previous findings is the flight phase with the highest power demand. If necessary, the return transition and landing would then have to be carried out with 6 drives. Another possibility would be a landing like a conventional aircraft, which would even be conceivable as a glider without any propulsion at all. A prerequisite for this, however, would be an appropriately constructed landing gear, which has not yet been designed.

Using figure 5.5, we can estimate that the maximum thrust achievable by each of the 6 remaining propulsion systems using their continuous power of $35\,\mathrm{kW}$ would be $1600\,\mathrm{N}$ approximately, but at a rotational speed of $2800\,\mathrm{min}^{-1}$. This would result in a thrust-to-weight ratio of 1.22, which is rather low but might be sufficient for an emergency landing. A prior condition to this calculation is that the motor allows a rotational speed of $35\,000\,\mathrm{min}^{-1}$ in emergency situation, which is technically feasible according to SCIMO.

6.3.2 Resume of Aerodynamic Loads

The largest aerodynamic side force is $129\,\mathrm{N}$, which multiplies with a maximum lever arm from propeller disc plane to tilt axis of $500\,\mathrm{mm}$ to $65\,\mathrm{Nm}$. Consequently, it can be concluded that a large distance between propeller disc plane and tilt axis does not have a significant impact on the bearing loads of the tilt mechanism concerning the aerodynamically induced moments, which can reach approximately $650\,\mathrm{Nm}$. Regarding the yawing moment, the most important aspect is that it is almost linear dependent of the lateral advance ratio. It is a very strong moment that must be supported by the tilt axis bearings. Also the thrust poses an important load on the bearings.

The pitching moment is dimensioning for the tilt actuator, where large differences between the measured steady and simulated unsteady loads were found. A tilt actuator must be capable to support these high unsteady loads under all circumstances. However, it may be useful not to define dynamic loads as continuous loads that the actuator must be able to work against.

6.3.3 Inertia Multi-Body-Simulation

A basic Multi-Body Simulation was conducted to ascertain whether the inertia of the rotating propeller would impose a substantial load on the tilt actuator. In this model, a distance of $465\,\mathrm{mm}$ between the tilting axis and the propeller plane, a rotational speed of $2400\,\mathrm{min}^{-1}$ for the propeller and $30\,000\,\mathrm{min}^{-1}$ for the motor were assumed. The constraint torque resulting from a smooth 10-second tilt from vertical to horizontal is shown in figure 6.10 and is not significant compared to the aerodynamic loads. The remaining torque of somewhat more than $60\,\mathrm{Nm}$ represents the static torque induced by the distance between the center of gravity and the tilting axis.

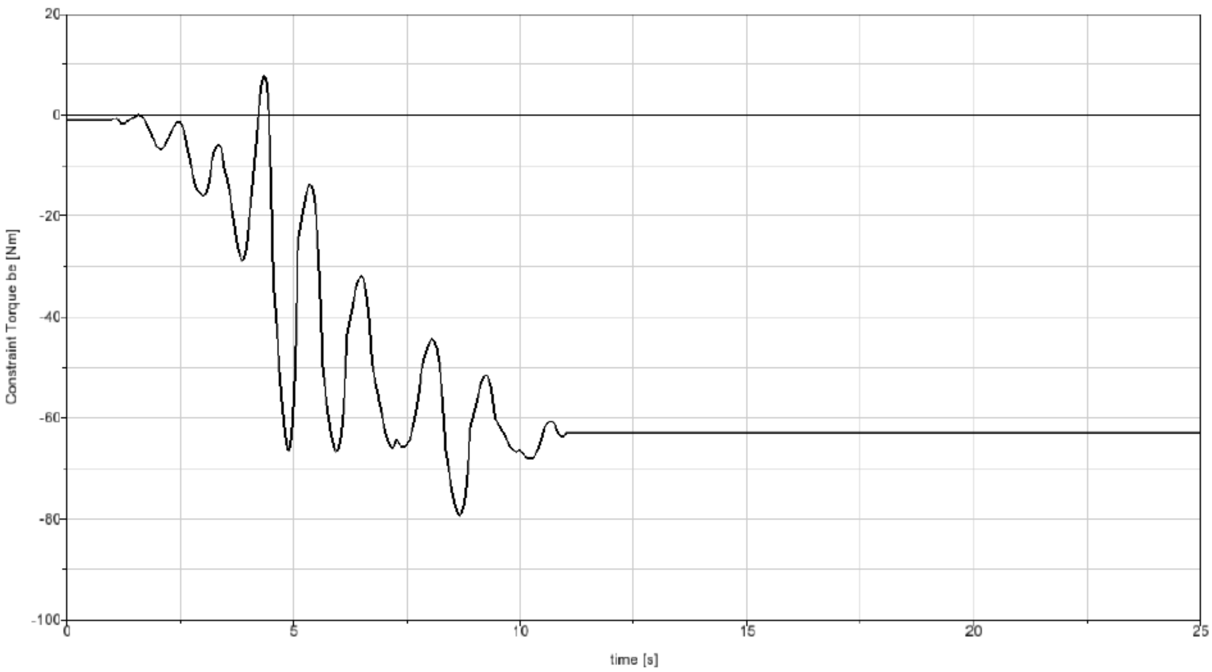

Fig. 6.10: Multi-Body-Simulation tilting constraint torque

6.3.4 G Loads

Even though no maximum g-loads have been specified in the project yet, the wing of the ALBACOPTER® 0.5 is designed for +5 g. Therefore, the swivel actuators should also be designed for this. If the tilt axis is in the center of gravity, there are no loads on the tilt actuator; if there is a distance, g-loads must be taken into account unless the propulsion system is in the upright position. For the front actuator, the acceleration due to gravity in horizontal mode can be easily absorbed by a mechanical stop, and for a half-tilted rotor, the aerodynamic moment acts against gravity. For the rear drive, which pivots downward, no mechanical stop is considered in the horizontal position. However, since the g-loads are below the maximum aerodynamic loads (assuming +5g and the torque of $60\,\mathrm{Nm}$ assessed in figure 6.10), the actuator should be able to bear them. Since the highest aerodynamic loads only occur at a very oblique inflow, when the g-loads on the swivel actuator can only be small due to the short lever arm, a superposition of the two torques is ruled out.

6.3.5 Imbalance of the Rotor

Based on the experience of testing the propulsion system of the ALBACOPTER® 0.5, where a propeller imbalance caused large vibrations, this section is dedicated to this problem. A propeller can and should be balanced statically and dynamically. A dynamic balancing report of a propeller of an ultralight was used to estimate the loads that occur [46]. The unbalance of $2\,\mathrm{g}$ on a radius of 112mm indicated in the report after balancing means a centrifugal force of less than $20\,\mathrm{N}$, which is negligible.

6.3.6 Boom Load and Design

To be able to design a possible connection of the tilt mechanism to the boom, a preliminary boom design must be available. Therefore, project partner LEICHTWERK AG was consulted to do a preliminary calculation of the boom's dimensions.

Since the loads were previously determined in the coordinate system of the drive train, which can rotate around the support boom, the design loads must be determined separately for the boom. To do so, it is important to know which loads can occur at which tilt angles. For clarification in figure 6.11 a boom-fixed coordinate system is introduced. The wall represents the connection to the wing. In this section, the dimensioning forces and moments are determined for each axis.

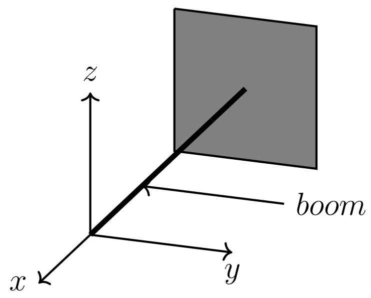

Fig. 6.11: Coordinate system for boom loads

The y-axis in the boom coordinate system in figure 6.11 coincides always with the propeller hub coordinate system introduced in figure 2.1 as it is the axis of rotation. So the bending moment around the y-axis is the maximum tilting moment given in 6.1 of $700\,\mathrm{N\,m}$, which occurs only at lateral inflow, for example at emergency back transition. The maximum force in y-direction is about $120\,\mathrm{N}$.

In x direction the largest torsional moment of the boom appears when the propeller is in hovering position at fast flight speed. It is the classical flapping moment and can reach up to $630\,\mathrm{N\,m}$. The maximum towing force, thus the thrust $T = F_{\mathrm{X}}$, achievable will be around $2200\,\mathrm{N}$.

The highest possible yawing moment around z-axis would occur in hover position induced by the motor. When the nacelle is in forward-flight position and the inflow is axial, the flapping moments mentioned above cannot occur. The flapping moment's dependency on the lateral advance ratio is shown in figure 6.4 a). So the maximum yawing moment is defined by the motor's peak torque and the gear ratio: $M_{\mathrm{Z}} = 23\,\mathrm{N\,m} \cdot 12.5 = 287.5\,\mathrm{N\,m}$.

All loads listed in this section are worst-case estimations and do not include safety factors.

LEICHTWERK calculated preliminary dimensions for the booms. It begins as shown in figure 7.7 at the drivetrain with a circular cross-section of $180\,\mathrm{mm}$ diameter and terminates at the wing connection with an elliptical cross-section measuring $230\,\mathrm{mm}$ in height and $207\,\mathrm{mm}$ wide. The wall thickness was determined to no less than $3.2\,\mathrm{mm}$.

7 Concept and Design

The purpose of this chapter is the application of the results of the previous chapters to decisions about the general concept of the propulsion system. It deals with the basic topology of the drivetrain, the tilt actuation system, the boom load and design and the structural connection to the propulsion system. Finally, some review calculations on the dynamic behavior and the mass of the concept are provided.

7.1 Definition of the Basic Topology of the Drivetrain

7.1.1 Spur Gear Topology

Initially, a spur gear was chosen to reduce the motor's high speeds for the propeller due to the perceived feasibility of realizing it within the given timeframe of this thesis. The gear comprised of two stages, as outlined in section 5.2.2, to limit the cross-sectional area. In the initial design presented in figure 7.1, the intent was to position the tilt axis close to the propulsion system's center of gravity, between the two gear stages. RSGetriebe GmbH was chosen as a partner for gear tooth system engineering and manufacturing, providing a preliminary calculation. Nonetheless, lubrication challenges emerged, necessitating an oil pump, along with manufacturing issues.

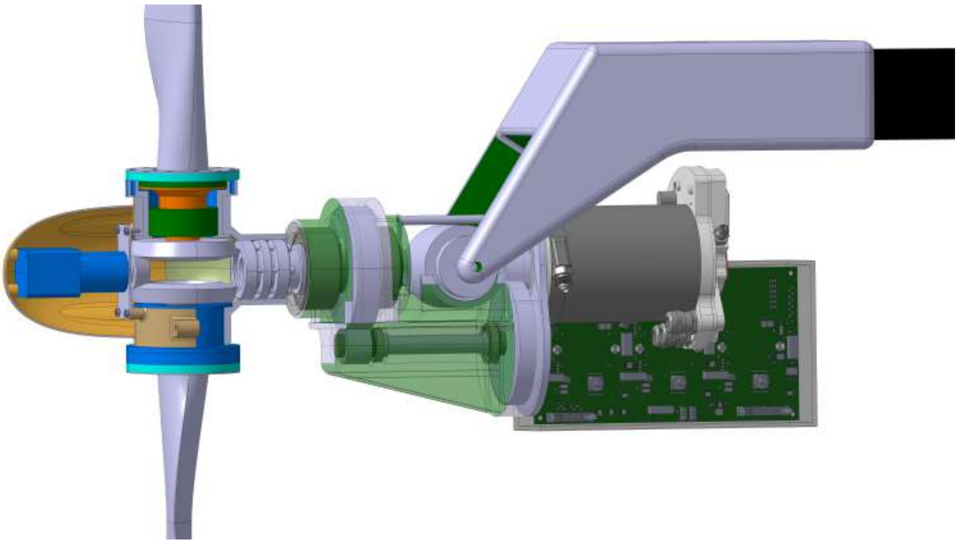

Fig. 7.1: First spur gear concept

7.1.2 Planetary Gear Topology

A planetary gear offers a more streamlined design, but high rotational speeds pose a challenge to engineers due to the centrifugal forces of the planets. Therefore, OEHLER GMBH was found as a partner who has a lot of experience with planetary gears.

There are many variations of planetary gears, but for the reduction ratio of 12.5 determined in section 5.2.2, the simplest configuration is sufficient to keep the complexity low. The sun gear is driven by the motor, the ring gear is fixed in the housing, and the planet carrier is connected to the output shaft. OEHLER estimates that the diameter of the entire gear will not to exceed $240\,\mathrm{mm}$, which isn't too large in relation to the motor, as illustrated in figure 7.2.

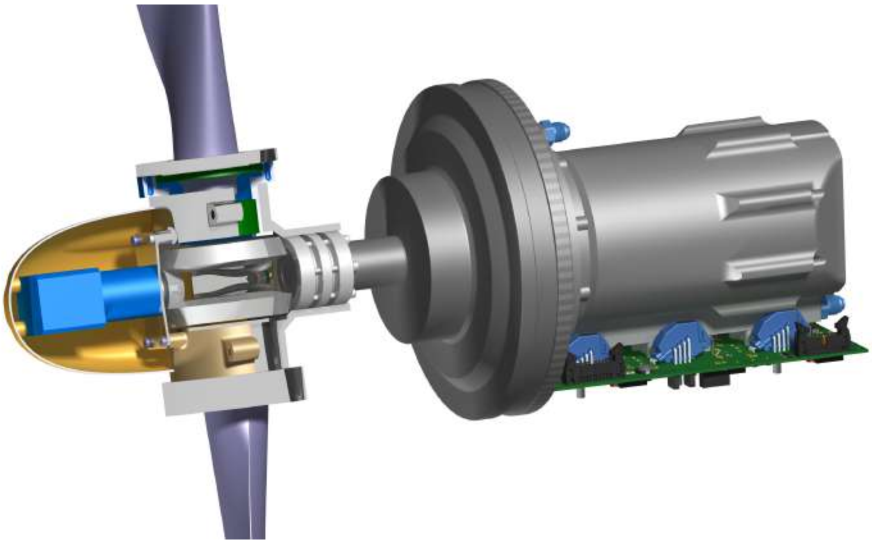

Fig. 7.2: Planetary gear concept

7.2 Definition of Tilt Axis Location and Selection of Tilt Mechanism

This section presents the pertinent options and decisions for the tilt mechanism based on the findings from the load investigation in chapter 6. The actuator needs to tilt the propulsion unit with precision and withstand all expected loads while maintaining minimal backlash.

7.2.1 Tilt Axis Location

Generally, it is important that the pitch axis and the propeller rotation axis intersect to prevent any tilting moment induced by propeller thrust. This constraint allows two reasonable locations for the pitch axis, which are explained in this section.

Tilt Axis Attached to Gear Housing

In this concept, the tilt mechanism bearing is an integral part of the planetary gear housing.

One advantage of directly connecting the motor to the planetary gear housing is that the motor housing only needs to support its own gravitational loads (g-loads). This simplifies motor housing design and construction, as it no longer needs to transfer aerodynamic loads from the propeller. Additionally, the tilt axis is located close to the center of gravity of the system to keep the tilting moment induced by g-loads low. The biggest advantage of this arrangement, however, is the short lever arms of the lateral propeller forces to the tilt axis. However, as demonstrated section 6.3.2, the lateral forces are not significant enough to cause substantial tilting or yawing moments, regardless of the length of the lever arms, in comparison to the aerodynamically induced moments.

Nonetheless, there are various disadvantages to take into account. Connecting the motor directly to the gear housing necessitates the integration of supplementary framework structure around the motor and peripheral components like the cooling system. As a result, this will enlarge the overall diameter of the system and potentially increase its weight due to the additional structure. Figure 7.3 depicts the concept at a medium tilt angle. It becomes evident that the structural framework constrains the space available for the cooling system.

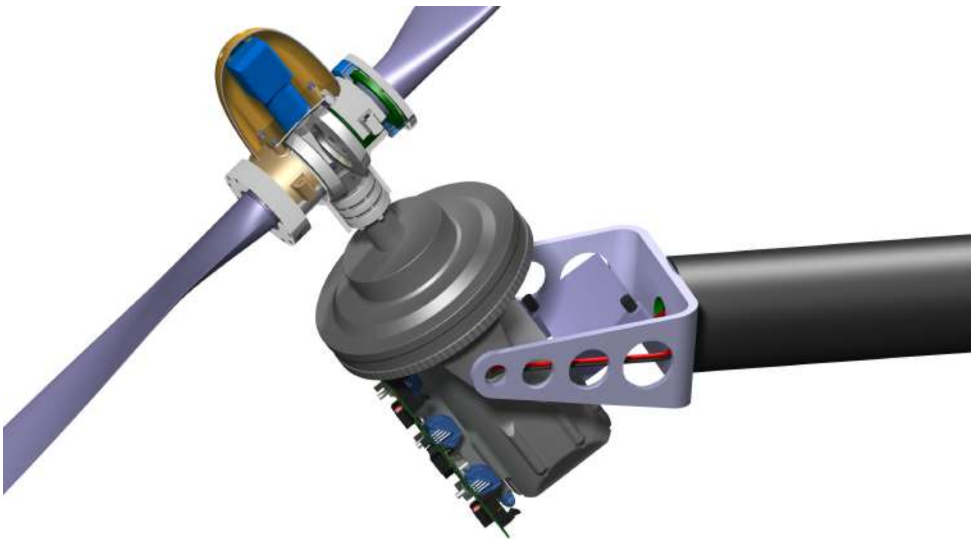

Fig. 7.3: Tilt axis connected to planetary gear housing

Tilt Axis Attached to Motor Housing

Attaching the tilt axis to the motor housing provides benefits such as eliminating the requirement for extra support structure, requiring less space, and allowing more space for peripheral devices listed in section 5.3. However, there are certain considerations to bear in mind. The motor housing must withstand the occurring loads, including g-loads, which are higher because of the distance to the center of gravity, and may require reinforcement. Simulating the motor's stiffness is challenging due to the contribution of stator sheet laminations. Additionally, the larger lever arm of lateral aerodynamic forces and g-forces can be challenging. Despite these challenges, SCIMO asserts that they can design the housing to withstand all loads thanks to the motor's large diameter, which is the main reason for further detailing this concept.

7.2.2 Tilt Mechanism

In this section, different feasible tilt actuation principles are presented and their advantages and drawbacks are discussed to take a decision.

As defined in section 6.1, the tilt actuator mechanism must be able to support a maximum unsteady tilting moment of approximately $650\,\mathrm{Nm}$ without damage. For continuous operation, a tilting moment up to $380\,\mathrm{Nm}$ should be achieved. Furthermore, large yawing moments have to be supported by the bearings. They can achieve $260\,\mathrm{Nm}$ in steady state and the time-resolved loads can go up to $520\,\mathrm{Nm}$.

For linear actuators, a lever arm of $100\,\mathrm{mm}$ was assumed to be realistic, as the whole diameter of the propulsion system will not be significantly more than the diameter of the planetary gear of $240\,\mathrm{mm}$. This would lead to forces of $3800\,\mathrm{N}$ for continuous operation and $6500\,\mathrm{N}$ holding force.

Industrial Linear Actuators

Industrial linear actuators are available in a wide range of load capacities and strokes. They are self-locking, come with encapsulation for harsh environments and a controller for direct connection to the CAN bus for easy integration. However, it is important to note that linear actuators that can support the estimated loads, have a weight of at least $6\,\mathrm{kg}$, which is a rather heavy weight.

Worm gear actuator

Worm gears are composed of a worm and a worm wheel, and they can achieve very high reduction ratios with a single pair of gears. They are also self-locking, which means in case of an actuator failure the propulsion unit would remain at its current tilt angle . However, worm gears have low efficiency and high wear due to sliding contact between the teeth. This disadvantage is not significant as the tilt mechanism is only in operation two times per flight during the transition phases. Backlash can be eliminated by a so-called duplex worm, which means that the tooth thickness varies continuously. The backlash can be adjusted by moving the worm in axial direction [47]. However, the worm bearing needs to support high axial loading, which makes it heavy. This can be illustrated by an angle gearbox offered by LIEBHERR AEROSPACE, which is used as a wing fold actuator for the BOEING 777X. It weighs $4\,\mathrm{kg}$, but the output torque is limited to $357\,\mathrm{Nm}$.

Ball Screw Actuator

As industrial linear actuators are too heavy, a lightweight actuator based on a ball screw with a driven ballnut was designed. The concept shown in figure 7.4 consists of a ball screw, a double row angular contact ball bearing and an frameless inrunning torque motor that rotates the ballnut. However, this concept was not further investigated due to space constraints and a difficult encapsulation against the environment.

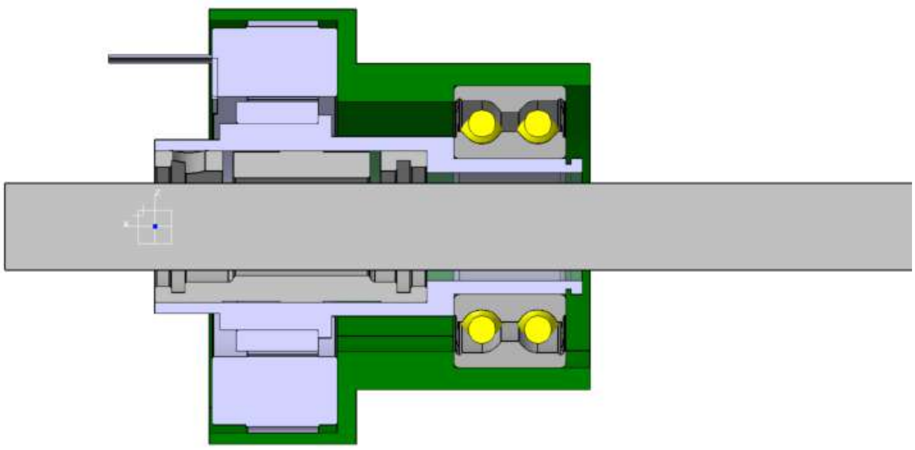

Fig. 7.4: Ball screw actuator sectional view

Strain Wave Gear

A strain wave gear was found as a possible solution for the tilt actuation system. It consists of a wave generator, which is elliptical shaped within its bearing and usually the driven element. Between the circular spline with internal teeth fits flexspline. It is a high strength, torsionally stiff yet flexible component with two external teeth less than the circular spline. They have no backlash throughout the service life, are short and lightweight while having a high torque capacity and high reduction ratios at high efficiency in one stage [48]. Additionally, they are easier to encapsulate than linear actors.

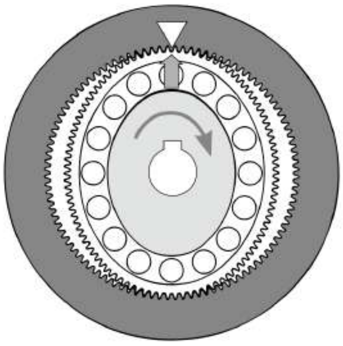

Fig. 7.5: Strain wave gear working principle

The initial concept illustrated in figure 7.6 utilized a strain wave gear provided by LEADERDRIVE with a reduction ratio of 160 and a maximum momentary torque allowance of 388 Nm at 1.24 kg weight [49]. The gear was paired with a T-MOTOR R80 outrunning torque motor, rated at 4 Nm and weighing 354 g. It is important to note that the wave generator bearing can support neither axial nor radial loads. As a solution, a lever was devised to exclusively support the gear's housing torque.

As the maximum torque could be too low for the loads assessed in section 6.3.2, there is the option to use two of the actuators or one motor and two of the gears connected by a shaft. A second, more lightweight option would be a CSD-2A strain wave gear provided by HARMONIC DRIVE with the same reduction ratio of 160 and a maximum momentary torque allowance of 694 Nm at 0.92 kg weight.

In total, combined with a ODRIVE motor controller, the actuator can achieve a weight of less than 2 kg.

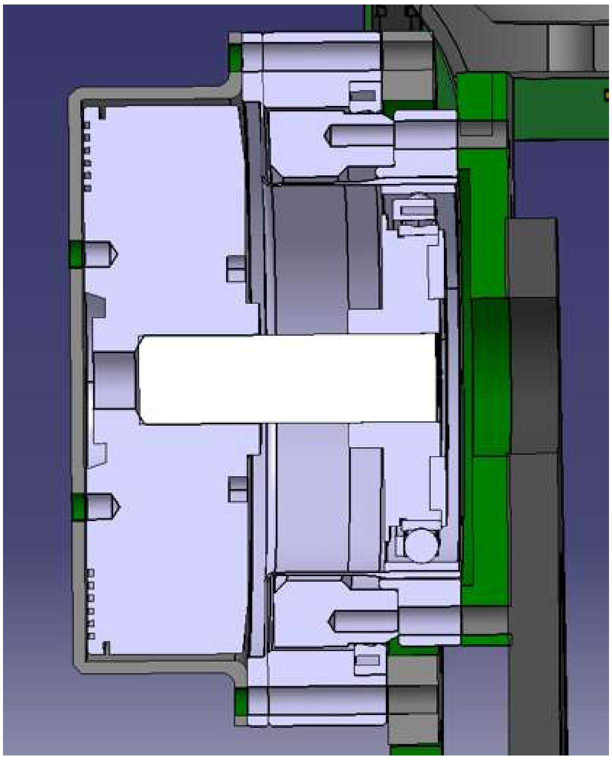

Fig. 7.6: Strain wave gear actuator sectional view

7.3 CAD Design of the Propulsion System Concept

There were several goals pursued with the CAD concept design shown in figure 7.7. The tilt axis should be as near as possible to the motor housing to avoid additional structure. The two bearing points were aimed to be as far apart as possible. However, more design work remains. A housing is necessary which provides protection against the environment.

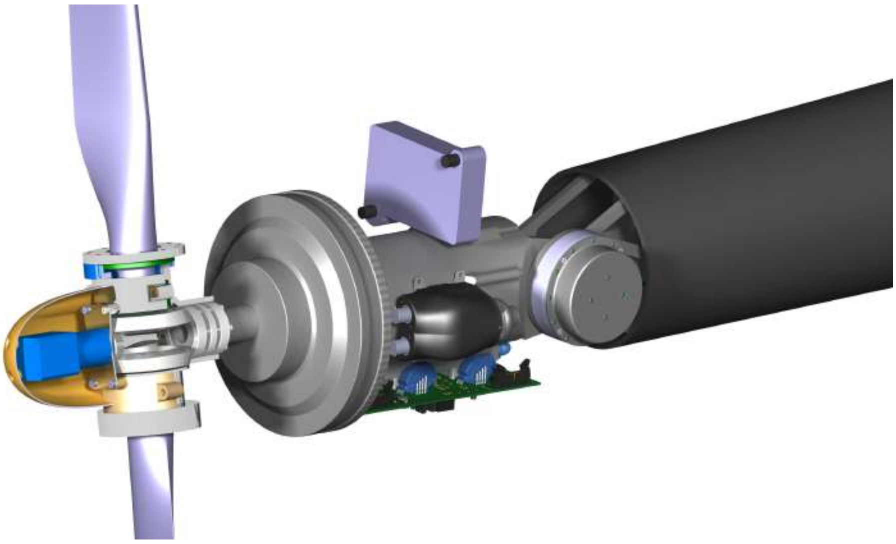

Fig. 7.7: ALBACOPTER® 1.0 propulsion system packaging concept

7.4 Review

In this section, the selected combination of motor and gear will be compared to an air-cooled aircraft outrunner motor with similar power with regard to dynamic behavior. As a comparable direct drive to the chosen SCIMO SY32 presented in table 5.3 the GEIGER ENGINEERING HPD40 (shown in figure 7.8) was selected which technical data can be found in reference [21].

Fig. 7.8: GEIGER ENGINEERING HPD40

7.4.1 Inertia and Dynamic Behavior

An outrunner electric motor has a larger rotor diameter than an inrunner, resulting in higher rotational inertia. In contrast, the internal rotor machine with gearbox has the disadvantage that the inertia must be multiplied by the square of the gear ratio $i = 12.5$ in order to relate them to the gearbox output. However, the inrunner with gearbox is able to deliver higher peak torque than an outrunner with similiar power and weight.

Tab. 7.1: Rotational inertia comparison

	SY32	**HPD40**	
Mass moment of inertia of motor	0.001	0.034	$\mathrm{kg\,m^2}$
Mass moment of inertia of gear (OEHLER)	0.000035	0	$\mathrm{kg\,m^2}$
Mass moment of inertia of drivetrain	0.162	0.034	$\mathrm{kg\,m^2}$
Mass moment of inertia of propeller and hub	0.25	0.25	$\mathrm{kg\,m^2}$
Total mass moment of inertia	0.472	0.344	$\mathrm{kg\,m^2}$

The mass moment of inertia of the propeller is determined using the two blades that weigh $739\,\mathrm{g}$ each and have a center of gravity radius of $280\,\mathrm{mm}$, measured from the blade's root. The blades are located in the current hub design at a distance of $57.5\,\mathrm{mm}$ from the rotational axis. For the hub, an estimated mass moment of inertia of approximately $0.08\,\mathrm{kg\,m^2}$ was calculated using CAD data. Therefore, the total mass moment of the propeller and hub in table 7.1 can be determined to

$$I_{\text{prop+Hub}} = 0.08\,\mathrm{kg\,m^2} + 2 \cdot 0.739\,\mathrm{kg} \cdot (0.3375\,\mathrm{m})^2 \approx 0.25\,\mathrm{kg\,m^2}. \tag{7.1}$$

As calculated in 7.1, the total mass moment of inertia of the geared drivetrain is about $45\,\%$ higher. The torque needed to overcome this inertia depends of the desired angular acceleration rate. According to section 2.1.4 a time needed to accelerate the propeller speed by $10\,\%$ can be calculated. Rising the velocity from $2000\,\mathrm{min}$ at $110\,\mathrm{N\,m}$ torque, which would be a typical hover situation, by $10\,\%$ to $2200\,\mathrm{min}$ the GEIGER ENGINEERING HPD40 requires $59\,\mathrm{ms}$. The SCIMO SY32 with a gear ratio of 12.5 and a estimated gear efficiency of $97\,\%$ requires only $51\,\mathrm{ms}$. So it can be concluded that the increase in inertia that results from a high gear ratio is more than offset by the benefit of a higher peak torque.

7.4.2 Mass Overview

FRAUNHOFER IVI estimated a total mass of every propulsion system of 22.5 kg. In this section shall be reviewed if this assumption is feasible.

Tab. 7.2: Assessed masses of the propulsion system components

	Weight/ kg	Total weight/ kg
Propeller	1.478	1.478
Hub	5.32	6.8
Electric Motor	6	12.8
ISC3 Inverter	0.8	13.6
Motor Controller	0.3	13.9
Coolant pump	0.37	14.27
Tilt actuator	2	16.27

The remaining weight of 6.23 kg seems not to be enough for the planetary gear, whose weight OEHLER estimates at 5 kg, the housing, heat exchanger, cables, coolant liquid and more. This result must be considered in the design of the overall aircraft concept.

8 Conclusion

In this chapter, the results and important findings of the thesis are summarized and an outlook on possible further research is given.

8.1 Summary

In the present work, a propulsion system for the Albacopter 1.0 was conceptualized. The selected propeller was simulated to determine its relevant characteristics. It was shown that in hover flight $2200\,\mathrm{min}^{-1}$ could be a reasonable speed and with$2800\,\mathrm{min}^{-1}$ the available maximum continuous power can be converted into thrust. Additionally, a method to simulate propellers whose geometry data are not available was tested. With the results of the simulation, relevant speeds and powers could be estimated to determine the topology of the propulsion system. For this purpose, a gear ratio of 12.5 was specified, which can be achieved with a planetary gear or a two-staged spur gear. Furthermore, the aerodynamic loads of the propeller, which experience oblique inflow during the transition, were determined. For this purpose, experimental and CFD simulation results from the literature were evaluated and qualitatively compared with our own tests. It was found that the resulting torques are far more relevant than the lateral forces. Other potentially critical loads were determined and set in relation to the aerodynamic loads. Especially the g-loads should not be neglected. Based on these results, the drive train and a tilt mechanism for the ALBACOPTER® 1.0 could be specified. As the main a planetary gear was determined. A strain wave gear was selected for the tilt mechanism because it combines all requirements. Finally, some retrospective calculations were conducted.

8.2 Outlook

Based on this work, the drive system can be developed further. Nevertheless, it is necessary to gain better understanding of the transition phase of the ALBACOPTER®. For this purpose, further wind tunnel tests with the ALBACOPTER® 0.5 are planned in order to test the propellers in combination with the wing and to determine the occurring forces and moments. A time-resolved measurement of the loads associated with the propeller's rotational position could be a valuable addition to current scientific knowledge.

Additionally, it is essential to test and validate the propeller hub. Measuring the propeller's performance in the chosen 2-blade configuration on a test bench will validate simulation results.

After these steps and a drive unit test on a test bench, the „iron bird“ presented in the introduction can be built up.

Appendix A.

Figures

List of Figures

A.1 Servo Current and Tilt Angle Plots From Experiments

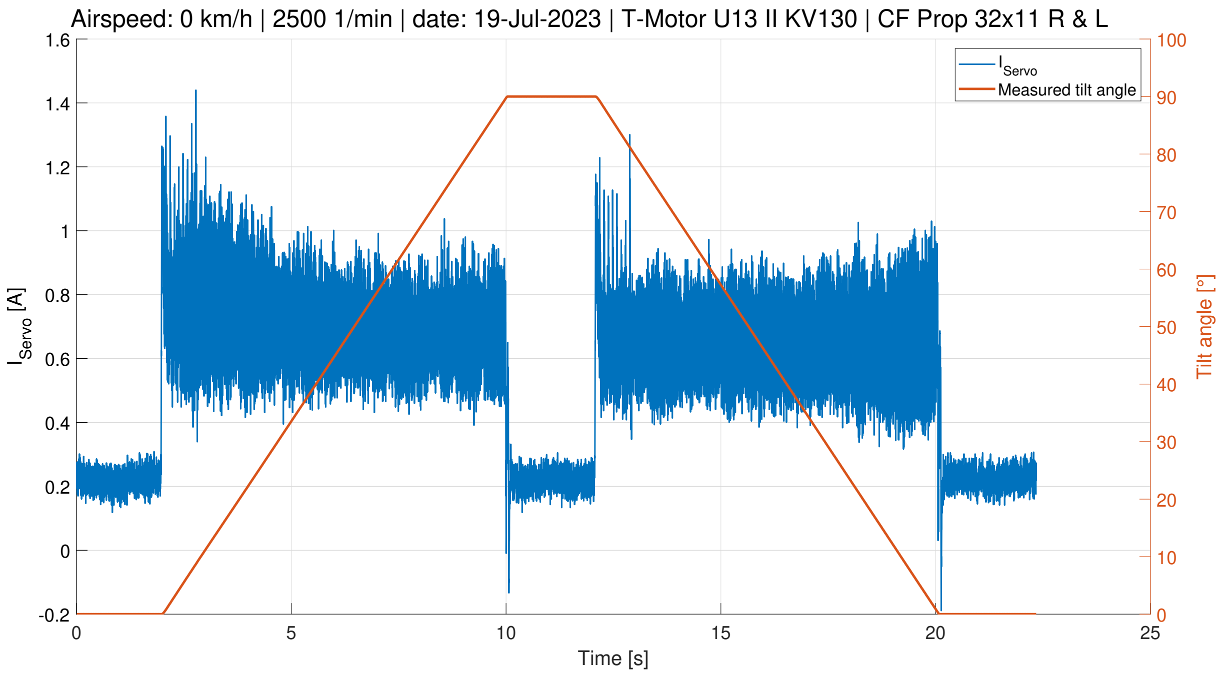

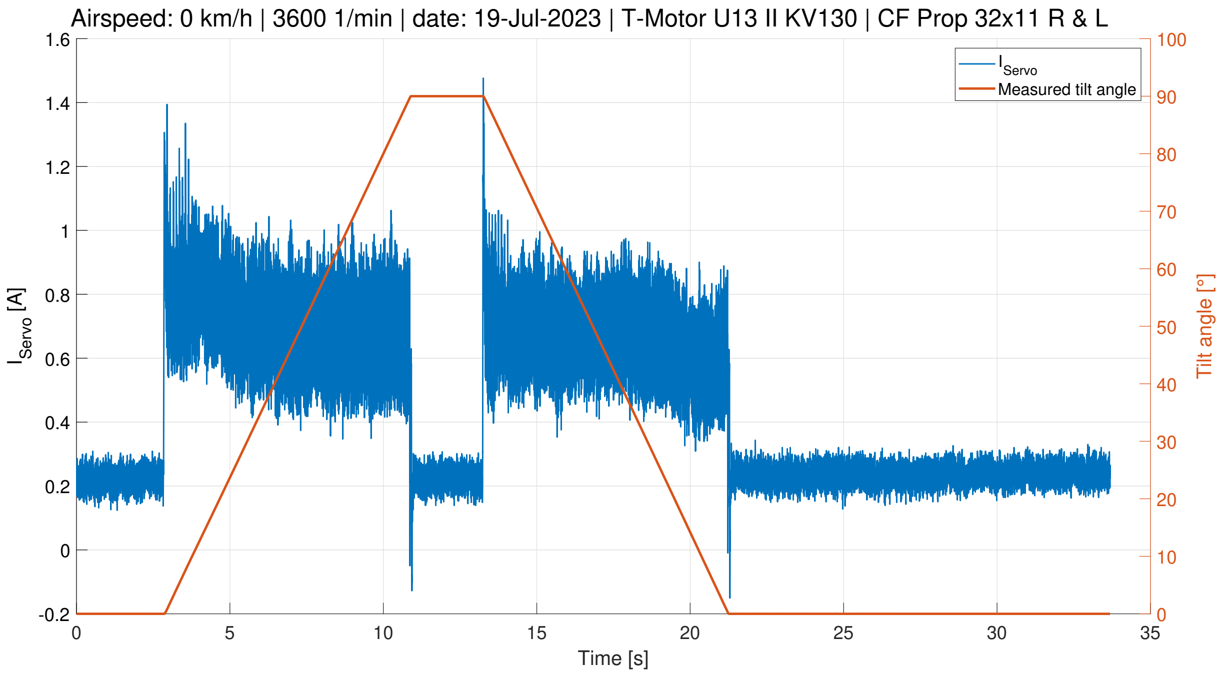

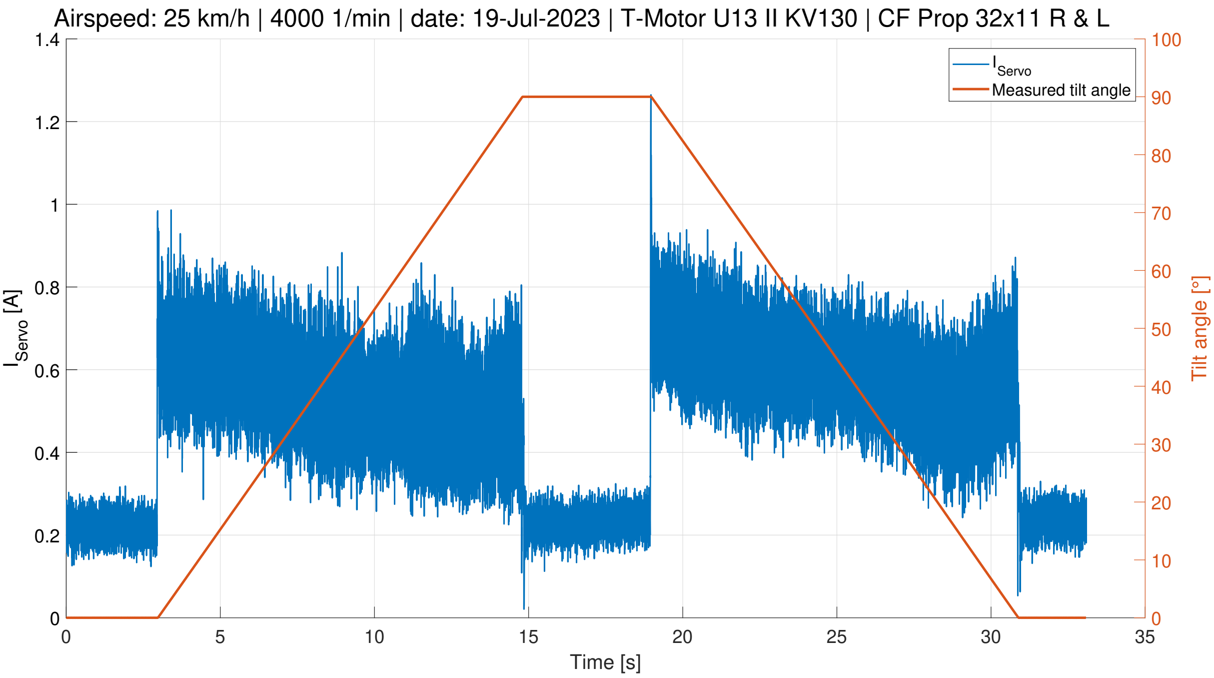
Airspeed: 25 km/h | 4000 1/min | date: 19-Jul-2023 | T-Motor U13 II KV130 | CF Prop 32x11 R & L
I_Servo
Measured tilt angle
I_Servo [A]
Tilt angle [°]
Time [s]

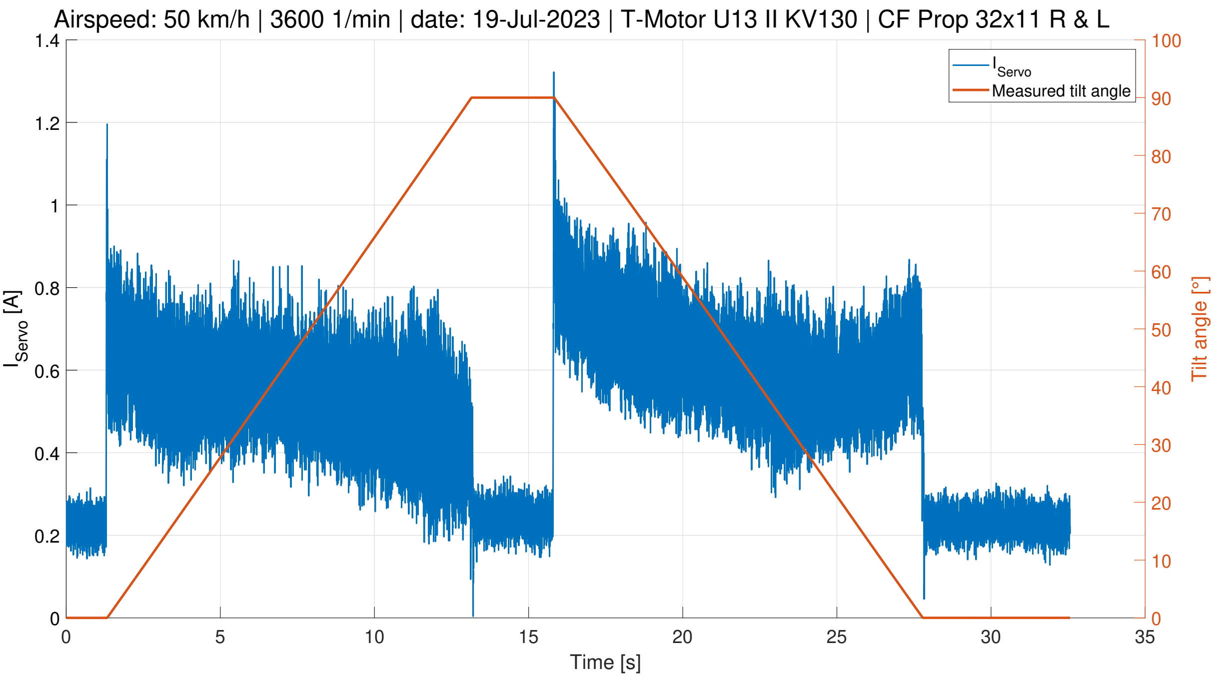
Airspeed: 50 km/h | 3600 1/min | date: 19-Jul-2023 | T-Motor U13 II KV130 | CF Prop 32x11 R & L
I_Servo
Measured tilt angle
I_Servo [A]
Tilt angle [°]
Time [s]

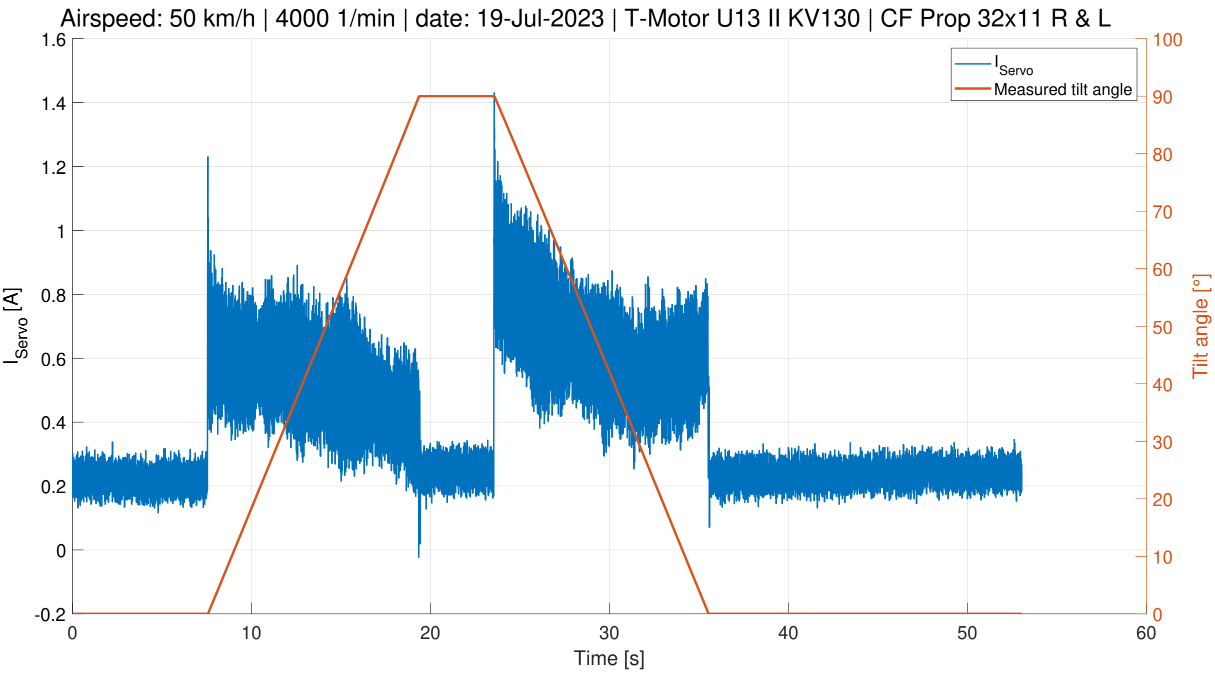
Airspeed: 50 km/h | 4000 1/min | date: 19-Jul-2023 | T-Motor U13 II KV130 | CF Prop 32x11 R & L
I_{Servo}
Measured tilt angle
I_{Servo} [A]
Tilt angle [°]
Time [s]
-0.2
0
0.2
0.4
0.6
0.8
1
1.2
1.4
1.6
0
10
20
30
40
50
60
70
80
90
100

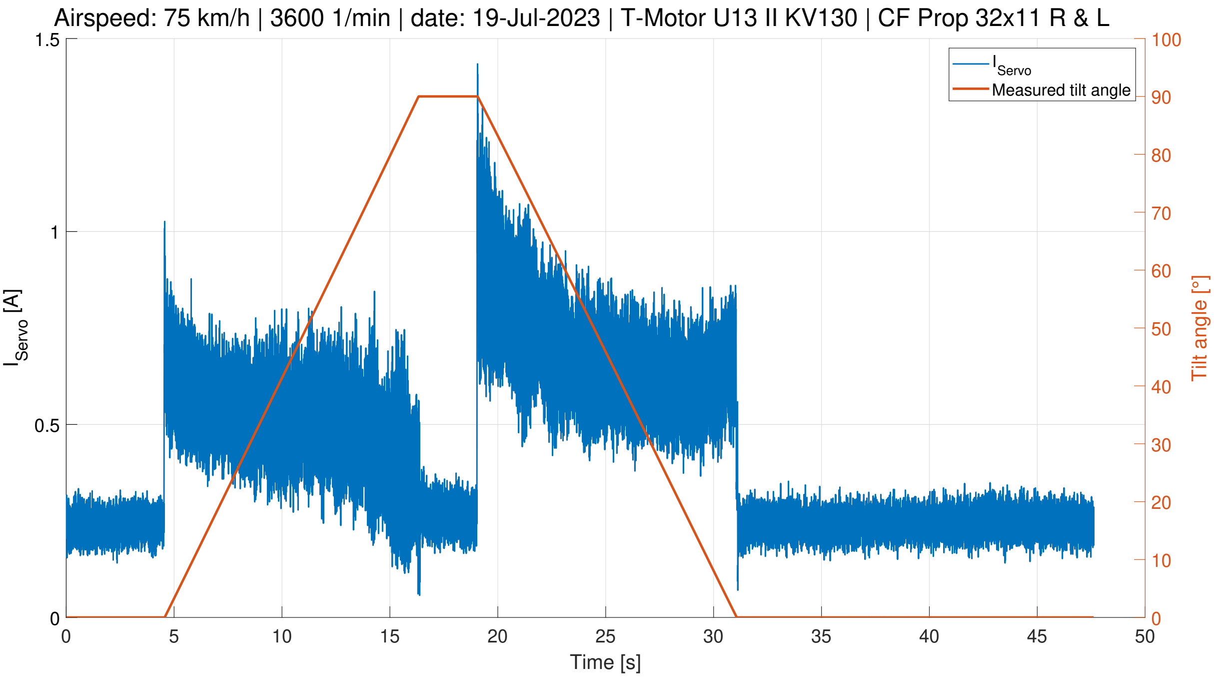
Airspeed: 75 km/h | 3600 1/min | date: 19-Jul-2023 | T-Motor U13 II KV130 | CF Prop 32x11 R & L
I_{Servo}
Measured tilt angle
I_{Servo} [A]
Tilt angle [°]
Time [s]
0
0.5
1
1.5
5
10
15
20
25
30
35
40
45
50
60
70
80
90
100

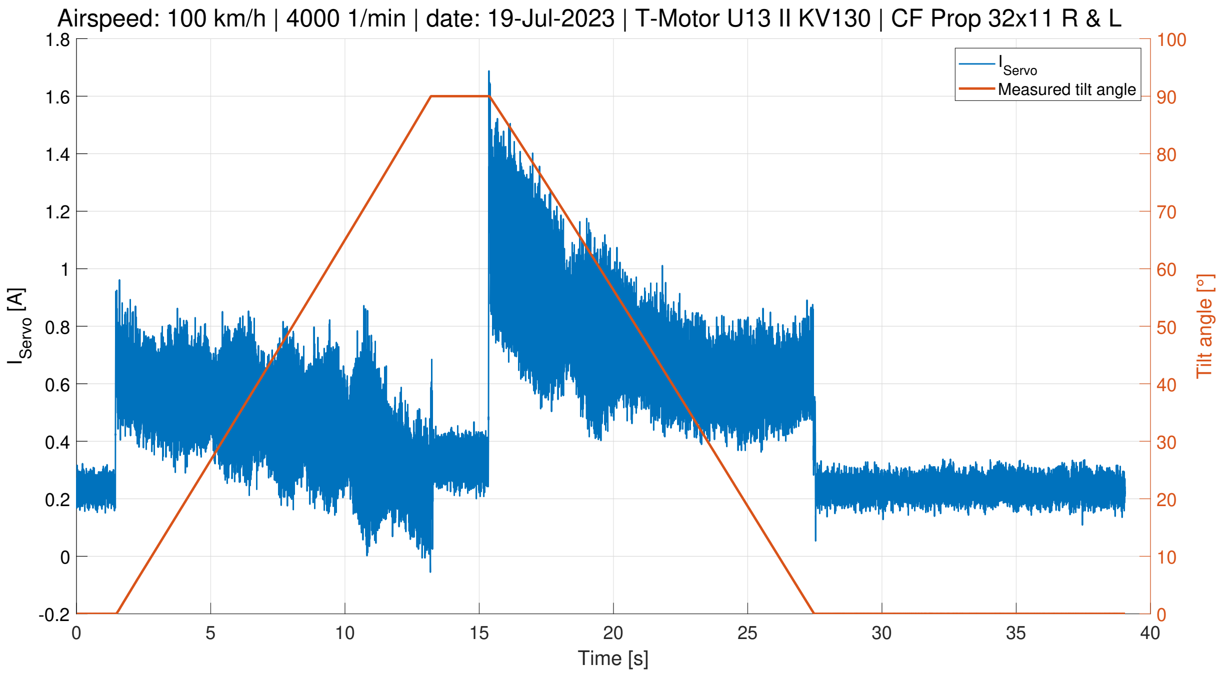
Airspeed: 100 km/h | 4000 1/min | date: 19-Jul-2023 | T-Motor U13 II KV130 | CF Prop 32x11 R & L
I_Servo
Measured tilt angle
I_Servo [A]
Tilt angle [°]
Time [s]

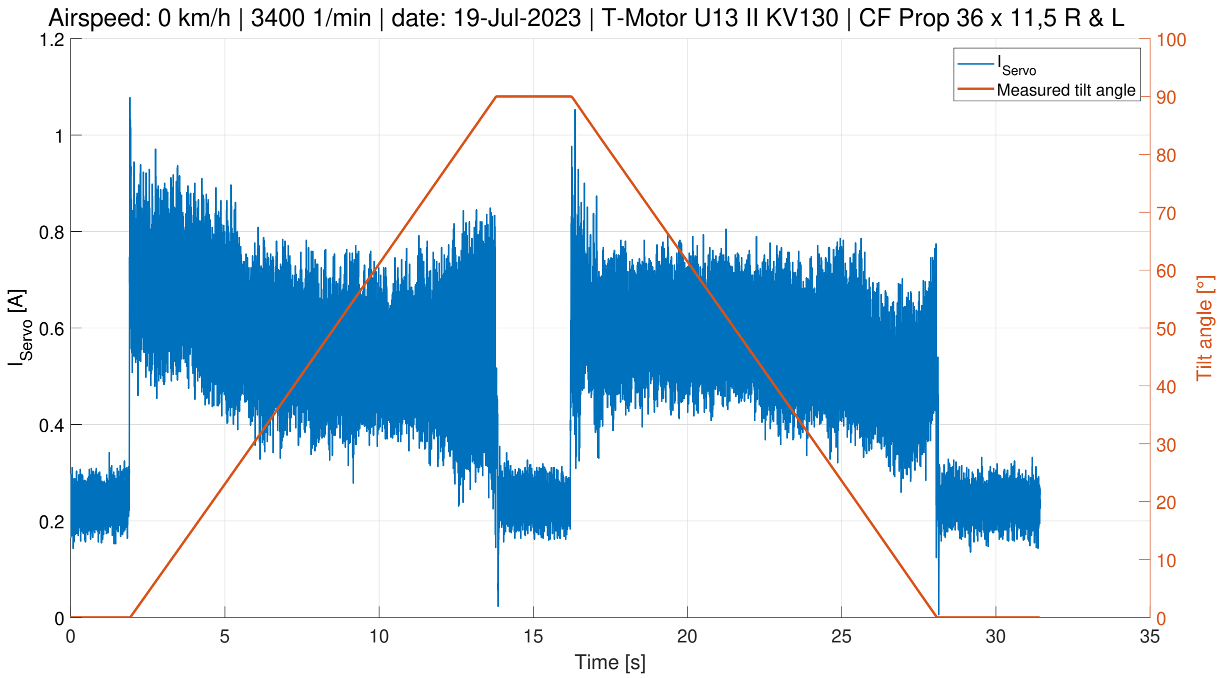
Airspeed: 0 km/h | 3400 1/min | date: 19-Jul-2023 | T-Motor U13 II KV130 | CF Prop 36 x 11,5 R & L
I_Servo
Measured tilt angle
I_Servo [A]
Tilt angle [°]
Time [s]

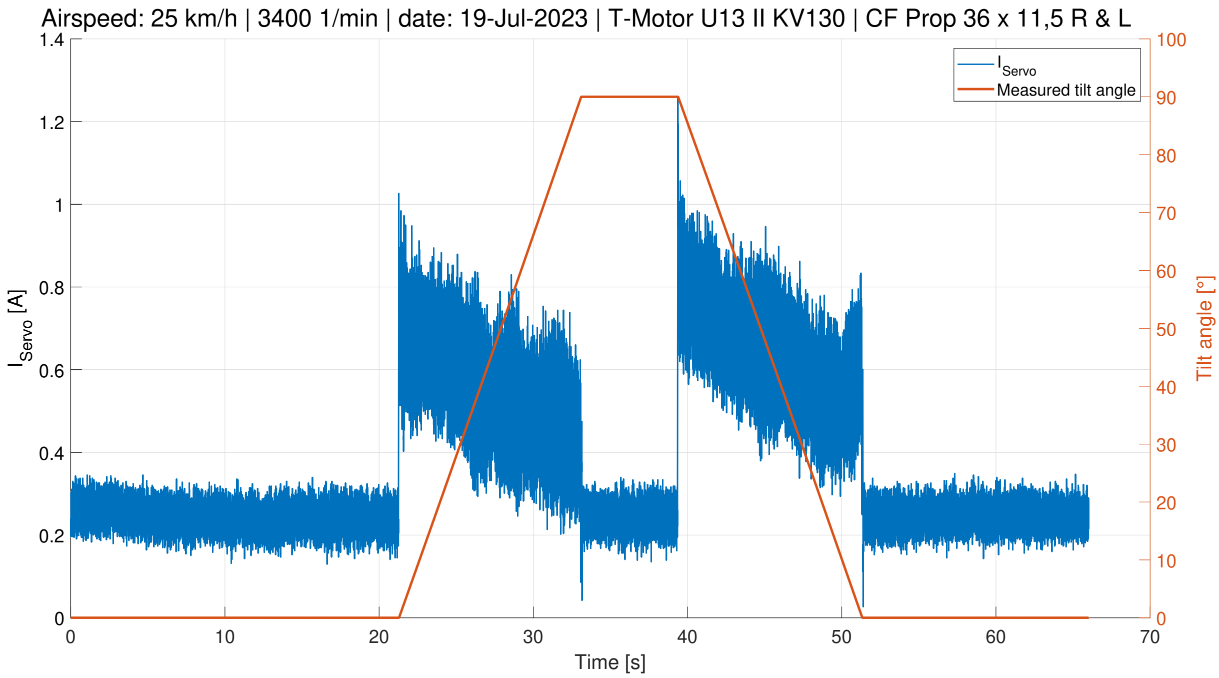
Airspeed: 25 km/h | 3400 1/min | date: 19-Jul-2023 | T-Motor U13 II KV130 | CF Prop 36 x 11,5 R & L
I_Servo
Measured tilt angle
I_Servo [A]
Tilt angle [°]
Time [s]

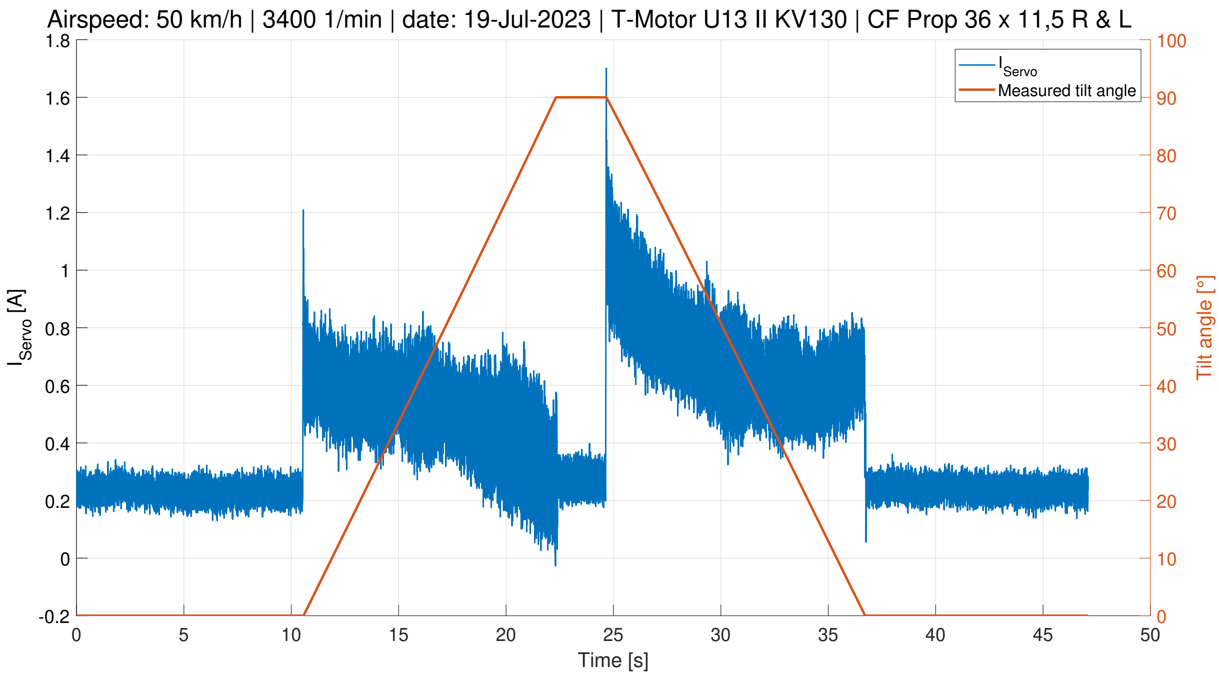
Airspeed: 50 km/h | 3400 1/min | date: 19-Jul-2023 | T-Motor U13 II KV130 | CF Prop 36 x 11,5 R & L
I_Servo
Measured tilt angle
I_Servo [A]
Tilt angle [°]
Time [s]

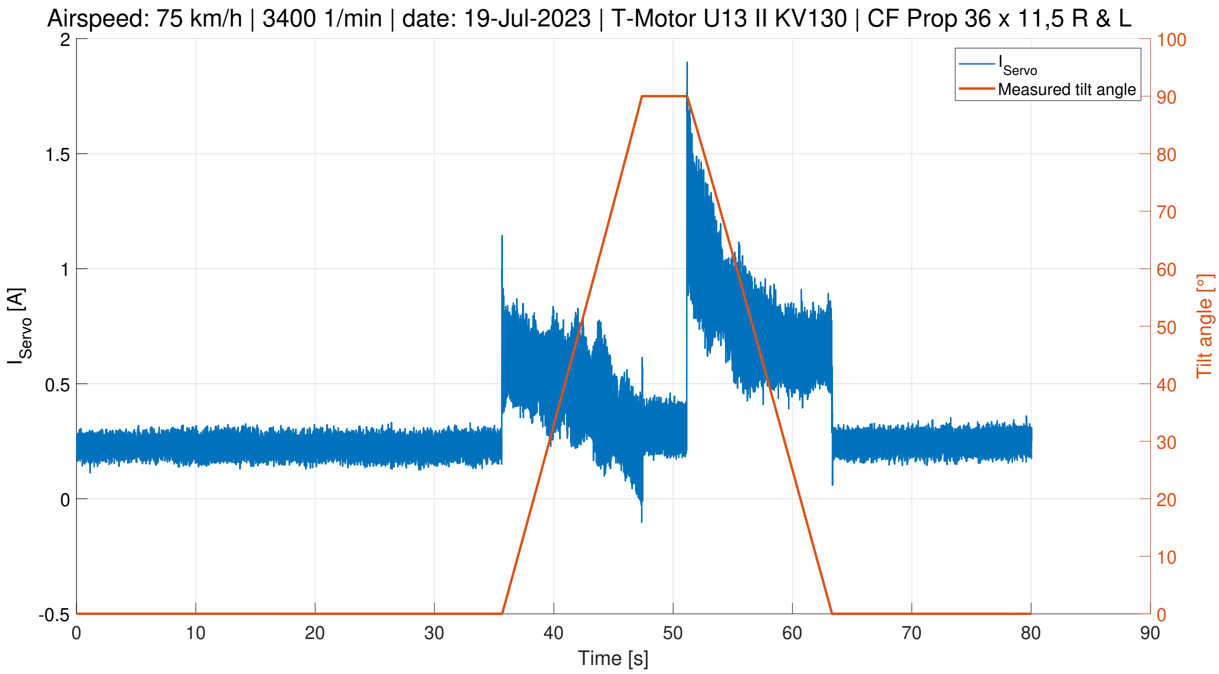
Airspeed: 75 km/h | 3400 1/min | date: 19-Jul-2023 | T-Motor U13 II KV130 | CF Prop 36 x 11,5 R & L
I_Servo
Measured tilt angle
I_Servo [A]
Tilt angle [°]
Time [s]

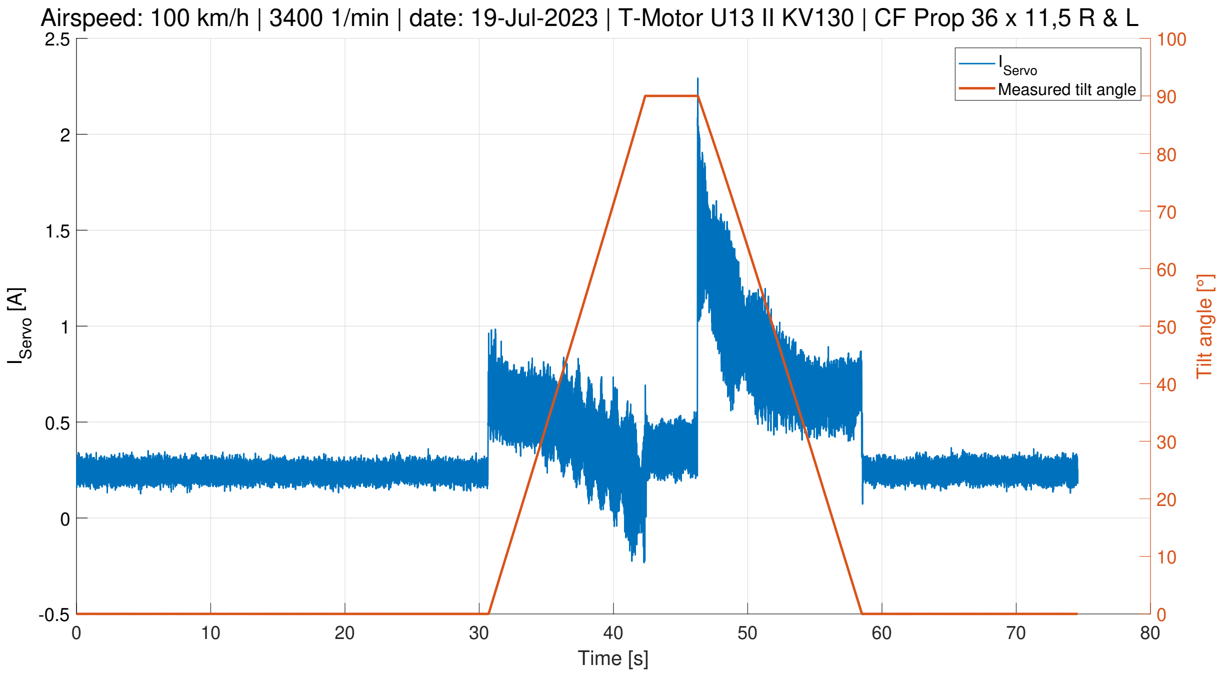
Airspeed: 100 km/h | 3400 1/min | date: 19-Jul-2023 | T-Motor U13 II KV130 | CF Prop 36 x 11,5 R & L
I_Servo
Measured tilt angle
I_Servo [A]
Tilt angle [°]
Time [s]

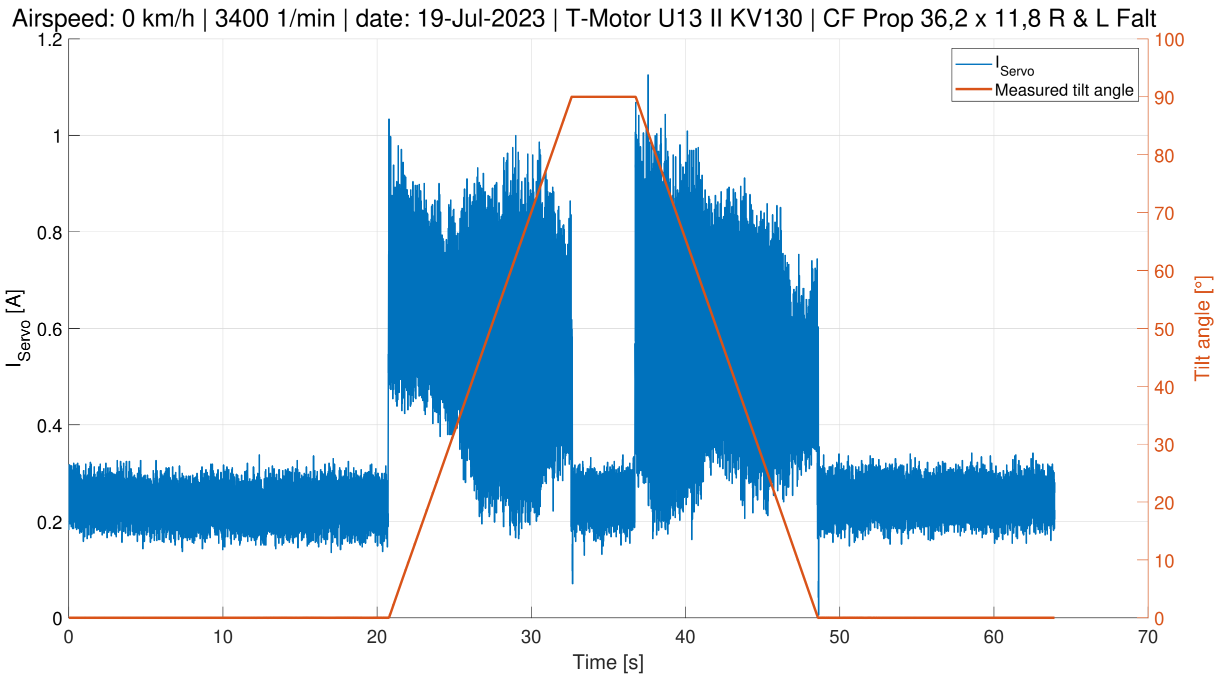
Airspeed: 0 km/h | 3400 1/min | date: 19-Jul-2023 | T-Motor U13 II KV130 | CF Prop 36,2 x 11,8 R & L Falt
I_{Servo}
Measured tilt angle
I_{Servo} [A]
Tilt angle [°]
Time [s]

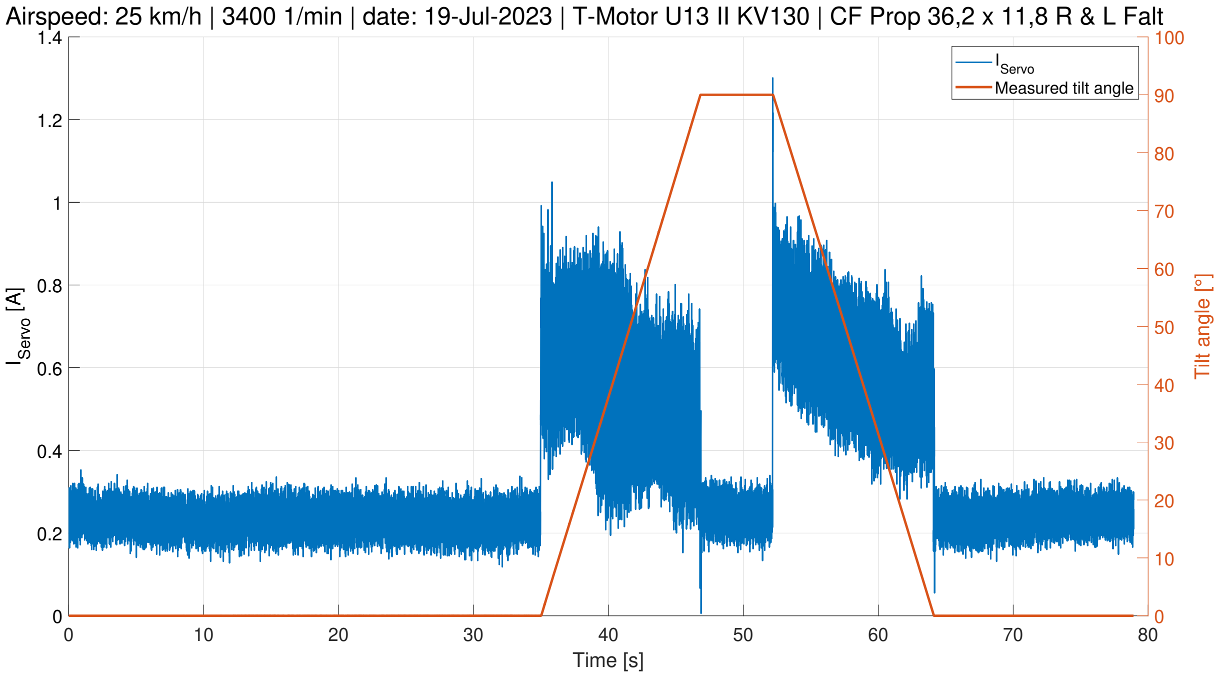
Airspeed: 25 km/h | 3400 1/min | date: 19-Jul-2023 | T-Motor U13 II KV130 | CF Prop 36,2 x 11,8 R & L Falt
I_{Servo}
Measured tilt angle
I_{Servo} [A]
Tilt angle [°]
Time [s]

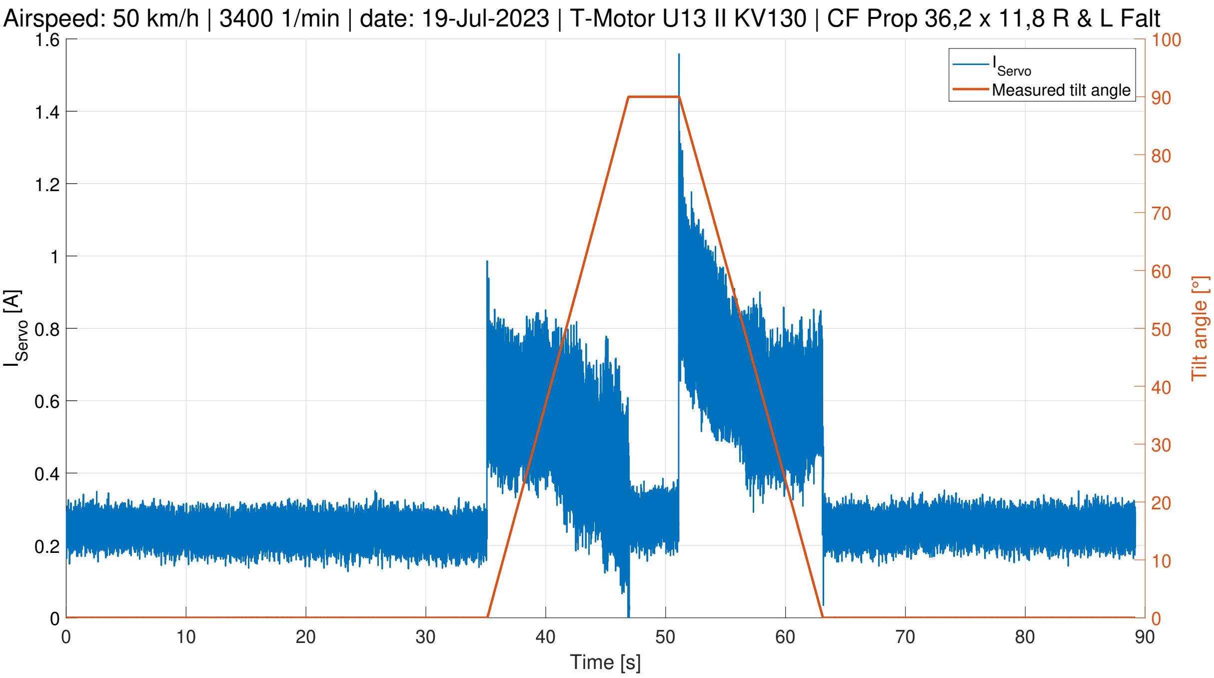
Airspeed: 50 km/h | 3400 1/min | date: 19-Jul-2023 | T-Motor U13 II KV130 | CF Prop 36,2 x 11,8 R & L Falt
I_Servo
Measured tilt angle
I_Servo [A]
Tilt angle [°]
Time [s]

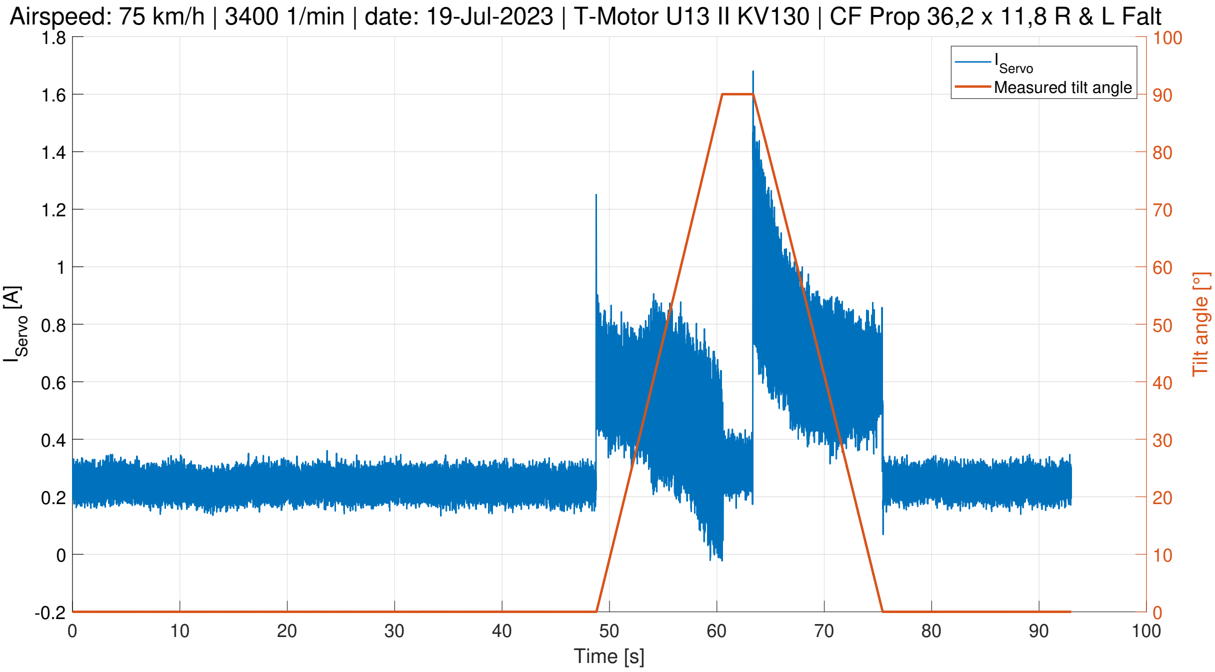
Airspeed: 75 km/h | 3400 1/min | date: 19-Jul-2023 | T-Motor U13 II KV130 | CF Prop 36,2 x 11,8 R & L Falt
I_Servo
Measured tilt angle
I_Servo [A]
Tilt angle [°]
Time [s]

Appendix B.

Tables

List of Tables

Appendix C.

Data Sheets

SciMo
Science for Motion

Datasheet

SY32.X002

(X002 is placeholder and will be replaced with final index upon ordering)

Machine		
Type		Permanent magnet synchronous
Performance		
Continuous torque	(calculated)	16 Nm @ 15.000 rpm
Continuous power	(calculated)	34 kW @ 25.000 rpm
Maximum torque	(calculated)	23 Nm
Maximum power	(calculated)	60 kW
Maximum speed	(calculated)	30.000 rpm
Electrical		
Nominal voltage DC-Link	(specified)	600V
Maximum current	(specified)	100 Arms
Number of pole pairs		3
Wiring		Y
Phase resistance	(calculated)	33,6mΩ
Induced DC-Voltage @ maximum speed	(calculated)	538 V
Materials		
Stator lamination		NO20
Rotor lamination		NO20 - 1200
Magnets		NdFeB
Mechanical		
Weight	(calculated)	≈ 6.0 kg
Rotor inertia	(calculated)	≈ 1 gm² (depending on shaft and interface)
Cooling		
Cooling fluid		Water/glykol
Flowrate (minimum)	(t.b.d)	6 L/min
Inlet temperature	(t.b.d)	Calculated for 65°C
Pressure loss @6L/min and 40°C	(typical)	To be calculated
Rotor cooling		Water/glykol
Sensors		
Position sensor		Hall Sensor with Sin/Cos output
Winding temperature		PT100 (4wires)
Rotor temperature		Infrared
Dimension		
Diameter	(without connector flange & cooling connectors)	124 mm (cylindrical part)
Overall Length	(without connector flange & cooling connectors)	226 mm
Interface		
Shaft interface		Inner Spline gear (cylindrical output shaft possible)

All data calculated. Result of prototypes might differ.

SciMo Elektrische Hochleistungsantriebe GmbH | Wikingerstraße 13 | 76189 Karlsruhe | www.sci-mo.de

Bibliography

[1] Fraunhofer ALBACOPTER® Lighthouse Project: Scalable Drone Concept, 2020. URL https://www.albacopter.fraunhofer.de/en.html.

[2] Nicholas K. Borer, Michael D. Patterson, Jeffrey K. Viken, Mark D. Moore, Sean Clarke, Matthew E. Redifer, Robert J. Christie, Alex M. Stoll, Arthur Dubois, JoeBen Bevirt, Andrew R. Gibson, Trevor J. Foster, and Philip G. Osterkamp. Design and Performance of the NASA SCEPTOR Distributed Electric Propulsion Flight Demonstrator. In *AIAA Aviation Technology, Integration, and Operations Conference*. 2016. URL https://ntrs.nasa.gov/citations/20160010157.

[3] Joby Aviation. Production Launch. URL https://drive.google.com/file/d/1Ri9lee8NOqdk9C0zS0Stzzm-saCBrIsQ/view.

[4] R. Jansen, C. Bowman, A. Jankovsky, R. Dyson, and J. Felder. Overview of NASA Electrified Aircraft Propulsion Research for Large Subsonic Transports, 2017. URL https://ntrs.nasa.gov/archive/nasa/casi.ntrs.nasa.gov/20170012222.pdf.

[5] Henry Andersen, Yuankang Chen, Mohammad M. Qasim, David G. Cuadrado, David M. Otten, Edward Greitzer, David J. Perreault, Kirtley, James L., Jr., Jeffrey H. Lang, and Zoltán Spakovszky. Design and Manufacturing of a High-Specific-Power Electric Machine for Aircraft Propulsion. In *forthcoming in AIAA Aviation Forum 2023*. 2023. URL https://hdl.handle.net/1721.1/150869.

[6] Robert Bruehl, Hartmut Fricke, and Michael Schultz. Air taxi flight performance modeling and application. 2021.

[7] Rudi Prinz. Systematische Auslegung eines Zielsystems und Entwicklung einer eVTOL-Antriebseinheit im Albacopter Projekt: Systematic design of objectives and

development of an eVTOL propulsion unit in the Albacopter project. Masterthesis, Karlsruher Institut für Technologie, Karlsruhe, 2023.

[8] Michael Cerny. *Aerodynamic Characteristics of Propeller Configurations under Non-Axial Inflow Conditions*. PhD thesis, Technische Universität München, München, 2022.

[9] Berend Gerdes van der Wall. *Grundlagen der Hubschrauber-Aerodynamik*. VDI-Buch. Springer Vieweg, Berlin and Heidelberg, 2., ergänzte, überarbeitete und korrigierte auflage edition, 2020. ISBN 978-3-662-60365-9.

[10] *Manual of the ICAO standard atmosphere: Extended to 80 kilometres (262 500 feet)*. ICAO, Montreal, 3rd ed. edition, 2002. ISBN 9291940046.

[11] Klaus L. Schulte. Der Propeller das unverstandene Wesen. 2007. URL `http://www.klspublishing.de/ejourns/e-Journ%20Al-05%20Der%20Propeller%20das%20unverstandene%20Wesen.pdf`.

[12] Snorri Gudmundsson. *General aviation aircraft design: Applied methods and procedures*. ELSEVIER BUTTERWORTH-HEIN, S.l., second edition edition, 2021. ISBN 978-0-12-818465-3. URL `https://search.ebscohost.com/login.aspx?direct=true&scope=site&db=nlebk&db=nlabk&AN=2464466`.

[13] Dirk Brunner. Stabile Drohne im Schwebeflug und Flug. URL `https://www.technik-consulting.eu/Analyse/Stabile_Drohne.html`.

[14] Gordon Strickert. Faktencheck Multikopter: Ähnlichkeiten und Unterschiede zu etablierten VTOL-Konfigurationen. In *DGLR-Netzpublikationen DLRK 2016*. DGLR, 2016. URL `https://elib.dlr.de/111091/`.

[15] Hans Albert Richard and Manuela Sander. *Technische Mechanik - Dynamik: Grundlagen - effektiv und anwendungsnah*. Vieweg(s) Fachbücher der Technik. Vieweg, Wiesbaden, 1. aufl. edition, 2008. ISBN 978-3-528-03995-0. doi: 10.1007/978-3-8348-9424-3.

[16] Michael Kügelgen and Ludwig Feuchtner. Futuristisches Eigenbau-UL mit "eVTOL-Genen": eMagic One. *Der Adler*, (07):6–8, 2023.

[17] Jason Louie Pereira. *Hover and Wind-Tunnel Testing of Shrouded Rotors for Improved Micro Air Vehicle Design*. Dissertation, University of Maryland, College Park, Md., 2008. URL http://hdl.handle.net/1903/8752.

[18] W. H. Reed, III. Review of propeller-rotor whirl flutter, 1967. URL https://ntrs.nasa.gov/citations/19670020798.

[19] C. Koch, J. Arnold, and H. Schmidt. Aeroelastische Untersuchung eines V-Leitwerks mit integrierten Antriebseinheiten, 2019.

[20] David Marten, Joseph Saverin, Robert Behrens de Luna, Sebastian Perez-Becker. QBlade Documentation, 2021. URL https://docs.qblade.org/.

[21] Joachim Geiger. Handbuch Elektrisches Antriebssystem komplett: Manual Complete electric drive system, 2023. URL https://www.geigerengineering.de/_Resources/Persistent/abd5ce77d0ad770032310a44e998c060f2a86200/Handbuch_Manual_E_Drive%20komplett_V1_2_21_DE_EN.pdf.

[22] Daan Moreels. This Inside-Out Motor for EVs Is Power Dense and (Finally) Practical. *IEEE Spectrum*, 2019. URL https://spectrum.ieee.org/axial-flux-motor.

[23] YASA Limited. About YASA: Our Mission Is To Accelerate Electrification, 2023. URL https://yasa.com/about/.

[24] H. Clyde McLemore and Michael D. Cannon. Aerodynamic Investigation of a Four-blade Propeller Operating Through an Angle-of-attack Range from 0 to 180 Degrees. URL https://ntrs.nasa.gov/citations/19930084170.

[25] H. A. Dwyer and W. J. McCroskey. Crossflow and Unsteady Boundary-Layer Effects on Rotating Blades. *AIAA Journal*, 9(8):1498–1505, 1971. ISSN 0001-1452. doi: 10.2514/3.49952.

[26] Hamid Amini and Sverre Steen. Experimental and Theoretical Analysis of Propeller Shaft Loads in Oblique Inflow. *Journal of Ship Research*, 55(4):268–288, 2011. ISSN 00224502. doi: 10.5957/JOSR.55.4.100044.

[27] Rubens Koleczko. Konzeptionierung und Entwicklung einer Vorrichtung zur realitätsnahen Nachbildung von Antriebslasten elektrischer Flugantriebe: Conception

and development of a device for the realistic simulation of propulsion loads of electric aircraft propulsion systems. Master's thesis, KIT, Pfinztal, 2022.

[28] B. Theys, G. Dimitriadis, T. Andrianne, P. Hendrick, and J. de Schutter. Wind tunnel testing of a VTOL MAV propeller in tilted operating mode. In *2014 International Conference on Unmanned Aircraft Systems (ICUAS)*, pages 1064–1072. IEEE, 27.05.2014 - 30.05.2014. ISBN 978-1-4799-2376-2. doi: 10.1109/ICUAS.2014.6842358.

[29] EMRAX. E-MOTORS. URL `https://emrax.com/e-motors/`.

[30] Tom Lombardo. Siemens Electric Aircraft Propulsion Unit: Inside the Digital Twin Design Strategy, 2018. URL `https://www.engineering.com/story/siemens-electric-aircraft-propulsion-unit-inside-the-digital-twin-des`

[31] Vertical Aerospace. VX4: Faster, quieter, greener, cheaper, 2023. URL `https://vertical-aerospace.com/vx4/`.

[32] Open House Event, 2022. URL `https://s27.q4cdn.com/936913558/files/doc_presentations/2022/11/Open-House-Event-Deck-for-Website.pdf`.

[33] EASA. Easy Access Rules for Unmanned Aircraft Systems (Regulations (EU) 2019/947 and 2019/945), 28.09.2022. URL `https://www.easa.europa.eu/en/document-library/easy-access-rules/easy-access-rules-unmanned-aircraft-systems-regulations-eu`.

[34] EASA. Special Condition Light UAS, 22.12.2021. URL `https://www.easa.europa.eu/en/document-library/product-certification-consultations/special-condition-light-uas`.

[35] European Union Aviation Safety Agency. Special Condition for VTOL and Means of Compliance: SC-VTOL-01, 2019. URL `https://www.easa.europa.eu/en/document-library/product-certification-consultations/special-condition-vtol`.

[36] European Union Aviation Safety Agency. Final Special Condition SC E-19 - Electric / Hybrid Propulsion System: SC E-19, 2021. URL `https://www.easa.europa.eu/en/document-library/product-certification-consultations/final-special-condition-sc-e-19-electric`.

[37] Helix Propeller. H60V 1,75m R-LTM-3. URL https://helix-propeller.de/3achs-ul-trike-gyro/alle-propeller/1759/h60v-1-75m-r-ltm-3/?number=HS10102.

[38] Richard Krüger-Sprengel. Manual for Propeller Type H60V. URL https://helix-propeller.de/media/pdf/40/cf/11/Handbuch-H60V-Englisch-Ausgabe-16-01-2016.pdf.

[39] André. xflr5. URL http://www.xflr5.tech/xflr5.htm.

[40] Boyd. Avoiding corrosion in liquid cooling systems, 2022. URL https://www.boydcorp.com/blog/avoiding-galvanic-corrosion.html.

[41] MT-Propeller. Electric constant speed MT-Propeller, 12.01.2023. URL https://mt-propeller.com/en/entw/pro_elec.htm.

[42] MOFLON. GT38109 series Long Life Rotating Slip Ring: Electrical Rotating Connector, 2023. URL https://www.moflon.com/gt38109.html.

[43] Geiger Engineering. FAQs. URL https://www.geigerengineering.de/en/avionics/faqs.

[44] Advanced Precision Composites. Technical Information. URL https://www.apcprop.com/technical-information/file-downloads/.

[45] M. Cerny, N. Herzog, J. Faust, M. Stuhlpfarrer, and C. Breitsamter. *Systematic Investigation of a Fixed-Pitch Small-Scale Propeller under Non-Axial Inflow Conditions*. Deutsche Gesellschaft für Luft- und Raumfahrt - Lilienthal-Oberth e.V, Bonn, 2021.

[46] Oliver Liedmann. Auswuchtbericht. URL https://ultraleicht.de/images/own/download/auswuchtbericht.pdf.

[47] Dengel, Brian. Eliminating backlash in worm gear pairs: Various techniques are available to minimize backlash in worm gear pairs., 2022. URL https://gearsolutions.com/departments/tooth-tips/eliminating-backlash-in-worm-gear-pairs/.

[48] Ovalo. Wellgetriebe, 2023. URL https://www.ovalo.de/technologie/wellengetriebe.

[49] LHSG High-Torque Hollow-Shaft Flexspline Strain Wave Gear. URL https://www.leaderdrive.com/strain-wave-gears/lhsg-high-torque-hollow-shaft-flexspline-strain-wave-gear-lhsg.asp.